Excitation and Readout Designs for High Field Spectroscopic Imaging

by

Joonsung Lee

Submitted to the Department of Electrical Engineering and Computer Science

in partial fulfillment of the requirements for the degree of

Doctor of Philosophy

at the

MASSACUHUSETTS INSTITUTE OF TECHNOLOGY

February 2011

Author.....
Department of Electrical Engineering and Computer Science
January 19, 2011

Certified by.....
Elfar Adalsteinsson
Associate Professor of Electrical Engineering and Computer Science
Associate Professor of Health Sciences and Technology
Thesis Supervisor

Accepted by.....
Terry P. Orlando
Chairman, Department Committee on Graduate Theses

Excitation and Readout Designs for High Field Spectroscopic Imaging

by
Joonsung Lee
Submitted to the Department of Electrical Engineering and Computer Science
on January 19, 2011, in partial fulfillment of the
requirements for the degree of
Doctor of Philosophy

Abstract

In this thesis we state and demonstrate solutions to three engineering problems that arise in magnetic resonance imaging RF excitation with parallel transmission (pTx) and magnetic resonance spectroscopic imaging (MRSI).

Recent work in parallel RF excitation in MRI has been demonstrated to offer dramatically improved flexibility for manipulation of magnetization preparation for imaging than is feasible with conventional single-channel transmission. We address two design problems that need to be solved before this emerging technology can be deployed in the clinical and research domain of human imaging at high field. First, we demonstrate a method for rapid and robust acquisition of the non-uniform fields of RF excitation due to arrays that are commonly used in pTx at high field. Our method achieves high-fidelity single-slice excitation and reception field mapping in 20 seconds, and we propose ways to extend this to multi-slice mapping in two minutes for twenty slices.

A fundamental constraint to the application of pTx is the management of the deposition of power in human tissue, quantified by the specific absorption rate (SAR). The complex behavior of the spatial distribution of SAR in transmission arrays poses problems not encountered in conventional single-channel systems, and we propose a pTx design method to incorporate local SAR constraints within computation times that accommodate pTx pulse design during MRI acquisition of human subjects. Our approach builds on recent work to capture local SAR distribution with much lower computational complexity than a brute-force evaluation, and we demonstrate that this approach can reduce peak local SAR by 20~40% for commonly applied pTx design targets. This thesis focuses on the design of excitation methods for high field system (7T parallel transmit (pTx) system) and fast readout and post-processing methods to reduce the lipid contamination to the brain. The contributions include fast B1+ mapping and pTx RF pulse design with the local SAR constraints for excitation. Regarding the readout method we developed a real time filter design, variable density spiral trajectory, and iterative non-linear reconstruction technique that reduce the lipid contamination. The proposed excitation methods were demonstrated using a 7T pTx system and the readout methods were implemented in a 3T system.

Our third contribution addresses a recurring problem in MRSI of the brain, namely strong contaminating artifacts in low signal-to-noise ratio brain metabolite maps due to subcutaneous, high-concentration lipid sources. We demonstrate two methods to address this problems, one during the acquisition stage where a spatial filter is designed based on spatial priors acquired

from the subject being scanned, and the second is a post-processing method that applies the brain and lipid source prior for further artifact minimization. These methods are demonstrated to achieve 20~40dB enhancement of lipid suppression in brain MRSI of human subjects.

Thesis Supervisor: Elfar Adalsteinsson
Title: Associate Professor of Electrical Engineering and Computer Science and
Associate Professor of Health Sciences and Technology

Acknowledgements

First of all, I would like to express my sincere gratitude to God and His son, my Lord Jesus Christ, who guided me to this place, made me to work with my great supervisor Elfar and Larry and nice colleges, Borjan, Trina, Kawin, Div, Lohith, Audrey, Berkin, Jessica, Rene, Khaldoun, Vijay, Azma, Wei. I really appreciate you have given me good ideas that I couldn't think of by myself. All of works I have done here are not actually what I did, but what you did through me.

I would like to thank my supervisor Prof. Elfar Adalsteinsson. You are the one who teach me how to do "research". I really appreciate your guidance, support, time and understanding on my research. I will remember my joyful moments working with you.

I am very fortunate to have the opportunity to work with Prof. Larry Wald. I thank him for his input and his reasoned advice, especially for broadening my perspective.

I thank Prof. Jacob White, who kindly gave his time to serve on my thesis committee.

I also want to thank my colleges; Borjan, Trina, Kawin, Div, Lohith, Audrey, Berkin, Jessica, Rene from MIT MRI Group, Khaldoun, Vijay, Azma, Wei from MGH, Hans-Peter Fautz and Matthias Gebhardt from Siemens. I want to thank especially Borjan whom I have spent most of my time with, at MIT, in Bay 5, and also in Erlangen.

Let me acknowledge the generous financial support of the Korea Foundation for Advanced Studies (KFAS). I'll do my best to contribute to the society.

I would like to thank my friends in the Korean church. You support me with your warm heart and pray. Thank you, dad, mom, and my brothers, Daesung and Hyosung. Thank you all.

Contents

List of Figures

Chapter 1

Introduction

Magnetic Resonance Imaging (MRI) is a widespread and important non-invasive imaging modality where the imaging signal arises from atoms with a nonzero nuclear spin angular momentum, such as the abundant ^{1}H in water. Over the last couple of decades, MRI has turned out to be a remarkably flexible imaging method, which in addition to providing high-contrast diagnostic results for radiological applications, also offers the means to map, for instance, local diffusion of water molecules in tissue due to Brownian motion, signal due to flowing blood, temporal variations in signal due to brain functional (fMRI), and is capable of mapping subtle signal variations due to low signal-to-noise ratio (SNR) moieties in compounds other than water (MR spectroscopic imaging).

Magnetic Resonance Spectroscopic Imaging (MRSI) offers the ability to spatially map the distribution of important compounds in the living human, with most applications to date concentrating on brain imaging [1], breast [2], and prostate [3, 4]. These signals of primary interest are separated from the dominant water reference by small frequency shifts, so-called chemical shift, and occupy a bandwidth of frequencies at 3T of several hundred Hz, and are often referred to by their frequency offset in units of parts-per-million, ppm, that's invariant to the strength of the main magnetic field, B0. For instance, a brain metabolite of high interest is N-acetyl-aspartate, NAA, a compound that is only found in neurons, and resonates at a frequency offset of 2ppm relative to water at 4.7ppm [1]. While the proton MRSI offers in vivo detection and mapping of spectrally-resolved compounds in human and animal subjects, this imaging modality is plagued by numerous technical challenges, including the low concentration of the

metabolites of interests (1-10mM) compared to the large water resonance for conventional MRI (~50M), the low SNR compared to MRI, limited spectral resolution of all of the signals of interest, inhomogeneities of the main (B0) and RF excitation B1 fields and the suppression of strong, unwanted signals from water and fat.

For brain MRSI in particular, estimates of brain metabolites using chemical shift imaging are severely hampered by strong lipid signals even though the interfering signal arises from regions outside of the brain, namely subcutaneous tissue in the skin, scalp, and bone marrow located inside the skull shown in Figure 1.

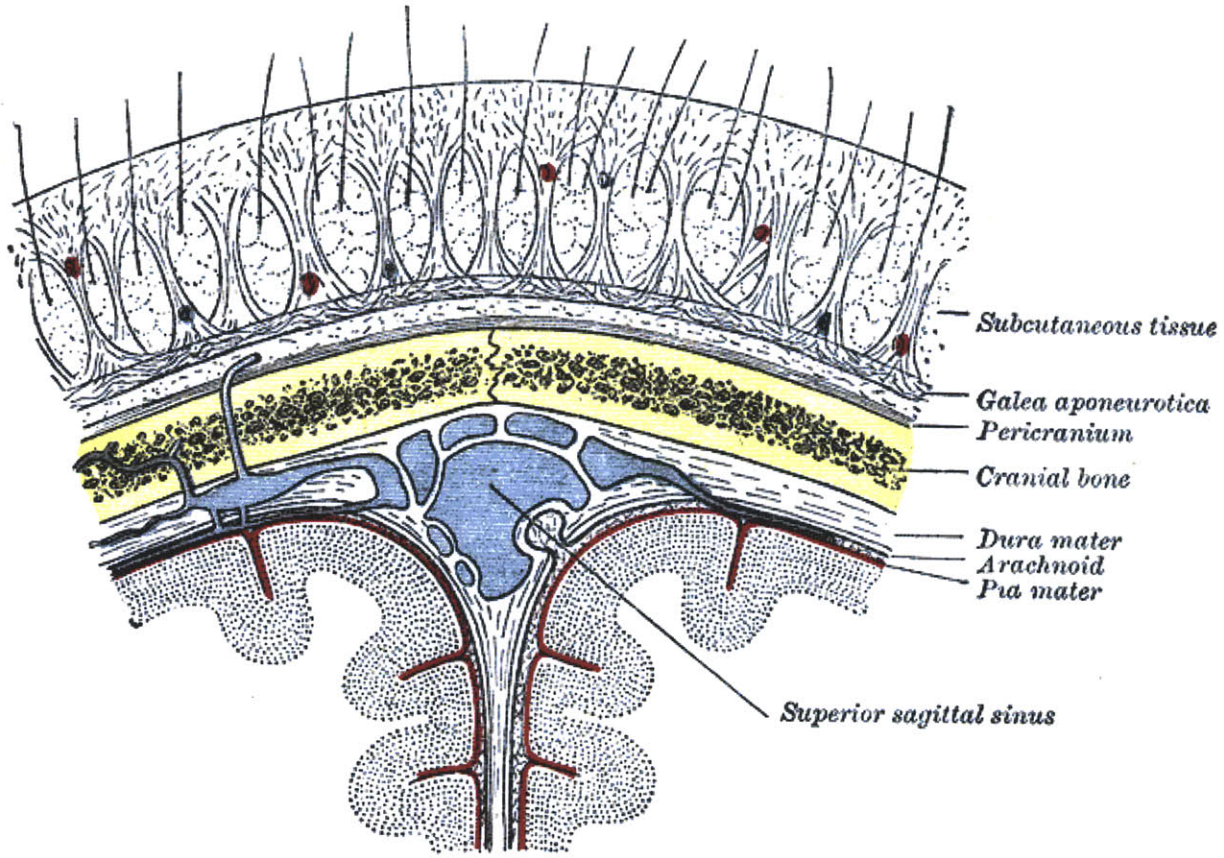

Figure 1: Meninges of the human brain[5]: interfering lipid signals are from the subcutaneous tissue in the skin and bone marrow in the skull

Membrane lipids within the brain are not visible at intermediate and long echo time (TE) due to their short relaxation times [1]. Since SNR in MRI is proportional to voxel size [6], the low metabolite concentration, and consequently low SNR in spectroscopic imaging, dictates

relatively large voxel sizes for reliable signal detection and quantification. The combination of a large voxel size and much higher concentration of lipids than proton brain metabolites, leads to the side lobes in the spatial impulse response as a significant contributor to interfering and undesired fat signals in spectra within the brain. This problem is all the more challenging due to the spatial proximity of the cortex to the source of the undesired signals, as well as the narrow spectral separation between lipids components in the 0.9-1.3 ppm range and the dominant NAA resonance at 2.0 ppm, which corresponds to a minimum separation of 86 Hz at 3T. The spectral peaks of NAA and nearby lipids overlap due to line-broadening from T2 and T2* as well as chemical shift due to B0 inhomogeneity.

1.1 Background

1.1.1 Two Phases of Magnetic Resonance Imaging (MRI): Excitation and Readout

MRI scans are composed of two phases: excitation and readout. These two phases are repeated per every TR (repetition time). Three kinds of magnetic fields, namely, the main magnetic field (B_0), Radio Frequency (RF) magnetic pulse (B_1) and gradient field (G) are used to create the MR signal and encode it during the readout phase. The strong external magnetic field, B_0, aligns a small portion of the spins along the applied field and rotate with the Larmor frequency $\omega=\gamma B_0$ where γ is called the gyromagnetic ratio. Most of the whole body system operates with a fixed B_0 field. During the excitation phase, the RF pulse excites the spins out of equilibrium and creates an MR signal in the transverse plane. RF field, B_1, is tuned to the Larmor frequency and excites only spins within a certain bandwidth. Gradient field, G, is added to the main field, B_0, to make the Larmor frequency depend on the spatial location. It enables the excitation of only a specified region such as a 3D slab and a thin slice. During the readout phase, it is used to encode spatially. The readout signal can be represented as the signal equation; the readout signal is a Fourier transform of the transverse component of the magnetization.

1.1.2 Parallel Transmit for High Field MRI

A high field system (7T) has intrinsic benefits of increased SNR, proportional to the main magnetic field, and increased chemical shift dispersion which results in a better spectral resolution for MRSI. However, the inhomogeneity of the RF excitation Field (B1+) is too severe at for human imaging at such high fields [7]. This field inhomogeneity, in turn, leads to inhomogeneous flip angle distribution over space and thus potential loss of both signal-to-noise ratio (SNR) and diagnostic contrast. Recent work has demonstrated great utility of parallel transmission (pTx) systems for radio frequency (RF) pulses in magnetic resonance imaging (MRI) for the purpose of generating much more flexible magnetization profiles including spatially uniform flip angle than is feasible with conventional single-channel RF systems [8-13]. Integral to the design of pTx RF pulses is the rapid and reliable mapping of both magnitude and phase of the B1+ for the transmit arrays.

The other critical challenge in pTx RF design is the minimization of the specific absorption rate (SAR), which is a measure of the deposited power per unit mass of tissue due to the RF pulse. Maximum values for SAR are specified by safety regulations and must be met both globally (e.g. power absorbed by the whole head or whole body) and locally (e.g. power absorbed per 10 grams of tissue). While global or average SAR values are readily measured and easily amenable to incorporation as constraints in the pTx RF pulse design [14], local SAR minimization during the design of pTx RF pulses poses a challenging optimization problem with a heavy computational burden.

1.1.3 B1+ mapping for single channel system

The B1+ map is a magnetic field transmitted to the subject by playing a unit voltage through the transmit coil and determines the flip angle of the excitation pulses. These B1+ maps vary from

subject to subject and also with respect to the relative location of the subject to the transmit coils. Thus, the B1+ maps should be measured for every subject to design the excitation pulse for high field system that has a large B1+ inhomogeneity. One of the major issues using high field system for in-vivo subjects in measuring B1+ is the lack of fast, robust, and reliable techniques.

Several quantitative B1+ mapping methods have been proposed and can be categorized into magnitude based methods and phase based methods. Magnitude based methods [11, 15-20] acquire two or more images using excitation pulses or saturation pulses with a varying flip angle. For these methods, the flip angle determines the magnitude of the images. By estimating the flip angle of the known excitation pulse, the B1+ map is acquired. Several problems for magnitude based methods include T1-dependence, long acquisition time, and sensitivity to large dynamic range of B1+. Alternatively, phase based methods [21, 22] encode the flip angle of the excitation pulse into the phase of the acquired images. The Bloch-Siegert method [21], which encodes B1+ in the phase of the image using an off-resonance RF pulse, is less sensitive to the dynamic range of B1+ but requires much more power in the RF pulse than the magnitude-based method such as double-angle method and could be limited by the global power or local SAR constraints to map B1+ especially for the region of very small B1+.

1.1.4 Spiral MRSI: Acquisition & Reconstruction

The metabolites of interest in the brain span frequencies within a spectral range of $800Hz$ on 3T systems. This implies that $800Hz$, corresponding to the temporal sampling of 1.25ms, is a sufficient spectral bandwidth for the purposes of MRSI. The current (Siemens) MRI systems allow temporal sampling that is as low as 1 μs for the readout and 10 μs for the gradient. Spatial and spectral encoding can be performed efficiently using time-varying readout gradients [23-36] by repeating a k-space trajectory for every period of 1.25ms and thus about 100 samples in spatial k-space can be acquired in one period. Compared to the conventional Phase Encoding (PE) MRSI, which acquires spectra for one sample in the spatial k-space per TR, the time varying

readout gradient can reduce the total scan time by a factor of 100. Among those approaches, spiral-based k-space trajectories [23] make excellent use of available gradient amplitude and slew rate.

Typically it is not feasible to cover the k-space spiral trajectory (kx-ky plane), especially for high spatial resolution, in one period of 1.25 ms with clinical gradient hardware. In order to overcome this problem, the spiral trajectory can be split into several interleaves: *temporal* and *angular* interleaves. Temporal interleaves are implemented by shifting the spiral trajectory along k_f (spectral) axis by the desired period once per each TR. Spending more time on the scanner, thus using several TRs, the desired spiral trajectory can be split into several temporal interleaves by increasing the period of the spiral lobe by a factor of the number of temporal interleaves. One spiral lobe can be played longer and, thus, the number of samples in one spiral lobe is increased. Figure 2 shows the implementation of the trajectory with two temporal interleaves.

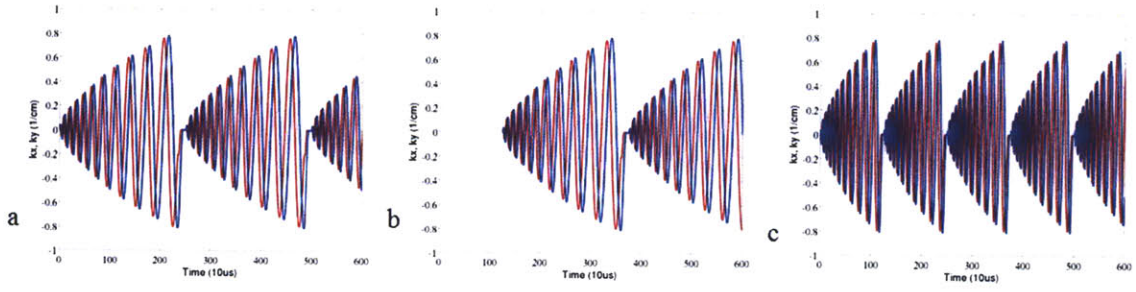

Figure 2: Temporal interleaves for spiral trajectory: kx (red), ky (blue), (a-b) individual temporal interleaf #1 and #2 whose period is 2.5 ms, (c) effective spiral trajectory by using the two temporal interleaves

Angular interleaves are implemented by rotating the spiral trajectory in k_x, k_y. For example, four interleaves implemented by rotating 0, 90, 180, 270 degrees are shown in Figure 3. The density of the trajectory is increased by a factor of the number of angular interleaves. The desired spiral trajectory can be split into several angular interleaves with sparser density.

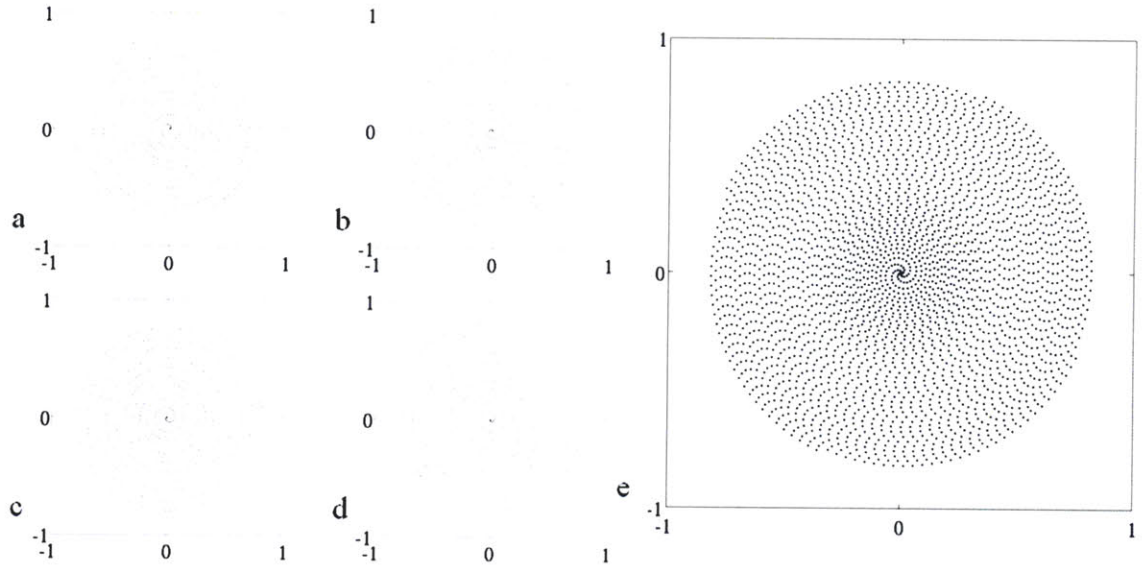

Figure 3: Four Angular interleaves for spiral trajectory in kx and ky: (a-d) individual angular interleaf (0, 90, 180, 270 degree), (e) effective spiral trajectory by using the four angular interleaves

For a single slice image with the in-plane resolution of $1cm^2$, the Field of View (FOV) of 24 cm*24cm and at the Nyquist sampling rate, the constant density spiral CSI scan takes only 20 seconds. For 3D imaging, the spiral trajectory can be generalized into a stack of spiral trajectory which samples inside a sphere shown in Figure 4.

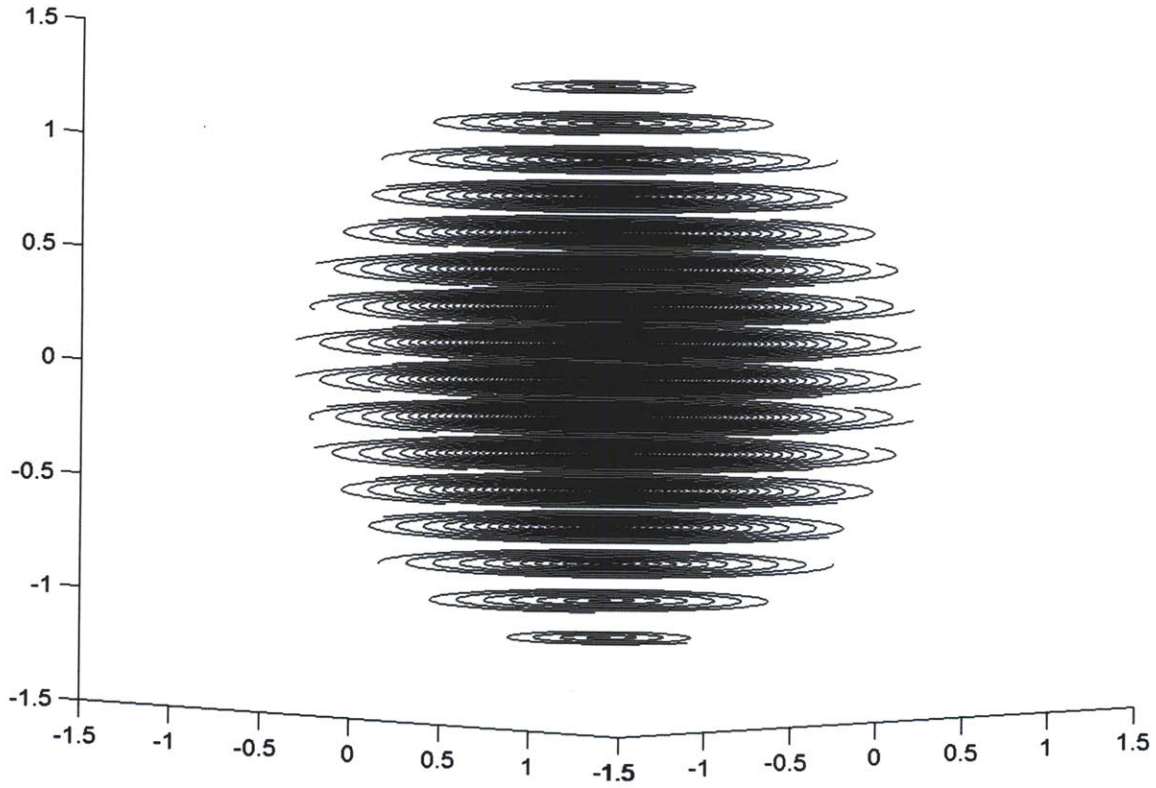

Figure 4: Stack of spirals trajectory for 3D imaging: sample inside a sphere, each slice for a fixed k_z (phase encoded) has an interleaved spiral trajectory

For 3D image with the Field of View (FOV) of 24 cm*24cm*12cm and Nyquist sampling rate, the constant density spiral CSI scan takes about 3.5 minutes for the voxel size of $1cm^3$, 6.5 minutes for $0.4cm^3$, 12.5 minutes for $0.2cm^3$.

For non-Cartesian (non-uniform) trajectories, the reconstruction of the MRSI is conventionally done by the gridding, zero-padding, followed by inverse Fourier Transform. The gridding [37] is a fast process that re-samples the k-space data into the Cartesian (uniform) grid. Then, zeros are padded on the k-space where the trajectory does not cover. By performing inverse FFT (Fast Fourier Transform), the spectra for all imaging voxels are reconstructed.

1.2 Contributions

In this thesis we propose and demonstrate solutions to three engineering problems that arise in

RF excitation design and image encoding for spectroscopic imaging at high field (3T and 7T).

1.2.1 B1 mapping

We first consider a problem in RF excitation that is motivated by the need for rapid and robust in vivo estimates of the spatial distribution of the RF excitation (B1+) and reception fields (B1-) for arrays of transmit- and receive array coils. Recent developments in the use of parallel transmit (pTx) technology have demonstrated the high degree of flexibility in the manipulation of magnetization beyond what is feasible for conventional single-channel systems [8-13]. Such pTx excitation methods, however, depend on high-quality field estimates, which pose a demanding imaging and reconstruction task for in vivo applications when combined with the need for rapid measurements in the presence of main field inhomogeneities, and potentially contaminating tissue contrast. We propose and demonstrate a fast multi-slice B1+ and B1- mapping method for pTx systems [38].

Unlike the previous approaches that simply estimate the B1+ of individual coils or individual modes, the proposed method takes advantage of the degree of freedom and ability to mitigate in the parallel transmit system. Large dynamic range of an image excited with a pTx system limits the SNR for B1+ and B1- estimate and increases the number of images required for reliable B1+ and B1- mapping. This dynamic range can effectively be decreased by optimally combining the eight images collected by the eight individual coils. In our proposed design, the coefficients for image combination are designed based on the initially acquired coil data during the mapping procedure, and they are optimized for the relative location of the subject to the coil and the region of interest. By estimating the B1- profile, which is independent to the transmit coils, through a properly chosen transmit mode, a combination of the transmit coils, the B1+ mapping for individual coils becomes faster and simpler. For single slice acquisition for eight-channel parallel transmit system, the B1+ and B1- mapping can be done in 20 seconds compared to 10 minutes presented in [39] for eight-channel 3T Body system, which uses a modified AFI method [40]. As an enhancement to this method, we have developed a compressed sensing [41] technique for B1+ mapping method that capitalizes on the smoothness (and therefore sparsity in

an appropriately chosen transform domain) of the B1+ map itself. Chapter 2 presents these approaches.

1.2.2 pTx Design with local SAR constraint

Another pTx design problem of critical importance concerns the management of power deposition in human tissue due to the applied parallel RF pulses during image acquisition. The specific absorption rate (SAR [W/Kg]) is a regulated safety parameter that quantifies the deposition of power per unit of tissue weight, and this constraint needs to be satisfied both locally (in any 1-g or 10-g tissue volume) as well as globally (e.g. over either the whole body or whole head).

Unlike conventional single-channel RF excitations whose maximum local SAR can be estimated by the measured global average RF power, pTx systems demonstrate a more complex spatial distribution of local SAR. Local SAR cannot be measured directly during an imaging experiment in human subjects, and needs to be estimated by other means. Typical approaches include numerical modeling of RF field distribution in spatially segmented tissue models with known conductivity and density. While such model-based estimates could theoretically be incorporated into pTx design methods by exhaustive evaluation of local SAR throughout the numerical body model, the computation required is prohibitive (proportional to the number of voxels, about five minutes for 300,000 voxels in an eight core CPU system). By building on recent work by Gebhardt et al [42] we developed a pTx design method that minimizes the peak local SAR in the parallel transmit RF pulse design in a very efficient way and achieves time savings over the naïve method of factor 3000. We demonstrate a 20~40% decrease of the peak 10g local SAR compared to a conventional transmit RF pulse design method with only a global power constraint, with computation times by a factor of 10. The means by which we incorporate the local SAR can be applied to several of the previously proposed pTx design methods. This method is presented in Chapter 3.

1.2.3 Lipid Suppression in MRSI

Our design problem in spectroscopic imaging is focused on the challenging task of lipid suppression in whole-slice or whole-brain MRSI of the brain.

Estimates of brain metabolites (~mM) using MRSI are severely hampered by strong lipid signals (~50M) even though the interference source is from regions outside of the brain, namely subcutaneous tissue, scalp, and bone marrow. Within-brain lipid signals arise from side-lobe ringing in the spatial impulse response of the image encoding, such that even a small spatial side-lobe (e.g. 10% of the main lobe peak) yields severe lipid artifacts in a range of chemical shift that interferes with the important NAA metabolite. While imaging at very high spatial resolution would effectively solve this problem, the low SNR of the desired brain metabolites dictate imaging with a large voxel size (on the order of 1 cm^3), which in turn suffers from severe lipid artifacts unless dedicated lipid suppression means are applied. One such approach is the reduction of the spatial side lobes without an SNR tradeoff employed an apodization with matched sampling density [43], which was demonstrated with a simple radial filter (Hanning) that constraints the main lobe and side-lobes of the point spread function (PSF) . In the current work, we extend these methods to optimize the apodization function for the subject being scanned by the collection additional prior data about the spatial extent of both the brain and the subcutaneous lipid sources during a short pre-scan. The filter constraints include the spatial impulse function main lobe and side-lobes, as well as lipid response inside the brain due to the surrounding lipid source. Through this procedure, we have enhance prior lipid suppression by over 10 dB [43]. Further, we demonstrate a post-processing lipid suppression within the brain through a non-linear iterative procedure that further reduces the lipid contamination by 10~20dB. Chapter 4 shows the details.

Chapter 2

Fast multi-slice B1+ and B1- mapping in Parallel Transmit System at 7T with adaptive optimal data combination

2.1 Introduction

The inhomogeneity of the RF excitation Field (B1+) is severe for human imaging at high field such as 7T [7]. This field inhomogeneity, in turn, leads to inhomogeneous flip angle distribution over space and thus potential loss of both signal-to-noise ratio (SNR) and diagnostic contrast. Parallel transmission (pTx) has been demonstrated to mitigate these B1+ and achieve spatially uniform flip angle [9, 11, 13, 44] and both spatially and spectrally [10]. Arbitrary shape can be excited with spiral trajectory [8] . In addition to this, local SAR can be reduced by properly combining the electric fields generated by the RF pulse transmitted to the coil [45]. Integral to the design of pTx RF pulses is the rapid and reliable mapping of both magnitude and phase of the B1+ for the transmit arrays.

The B1+ for individual transmit coils of the parallel transmit system is much more the inhomogeneous than the B1+ of the standard birdcage mode in the single channel system. Conventional magnitude-based, single-channel B1+ mapping methods such as the double-angle method [16, 19], multi-angle method [11, 17], saturation angle method [20, 46], and AFI [15] have a poor SNR efficiency or require more images to cover the increased dynamic range if they are applied on the individual TX channel. Alternatively, the Bloch-Siegert method [21], which encodes B1+ in the phase of the image using an off-resonance RF pulse, is less sensitive to the dynamic range of B1+ but requires more power in the RF pulse than the magnitude-based method such as double-angle method. If it is applied on the individual TX channel, the Bloch-Siegert method [21] requires a huge RF power which cannot be played due to SAR limit to map B1+ especially for the region of very small B1+.

For parallel transmit system, Fautz [46] presented a saturation angle method that measures the B1+ using one reference image and one saturation image. To increase the SNR efficiency, the excitation pulse is played on the birdcage mode but the saturation pulse is applied through the individual coil, in which we want to measure B1+. Compared to the B1+ mapping approach only using the individual coil alone, the method greatly improves the SNR especially for regions with a small magnitude of B1+.

The issue of the increased dynamic range of the B1+ in the parallel transmit system can be reduced by measuring the B1+ of the modes transformed by a matrix [39]. By a linearly combining properly, the dynamic range of all eight modes can be much smaller than the dynamic range of the individual coils. The constraint on this approach is that the transform matrix should have a low condition number. Simulation results in [39] at 3T show the reproducibility of the optimal matrix and suggests that once the matrix is tuned and then the same combination can be used for different subjects.

Setsompop [11] presented a two mode method (relative B1+ mapping method) that takes advantage of the receive profile estimate collected while estimating the B1+. The transmit profiles are transformed by the butler matrix [12]. For the birdcage mode, most uniform mode, multi excitation flip angle method [17] is applied to estimate the B1+. By fitting a predicted sine curve to the data, the magnitude of the B1+ as well as the receive profiles (B1-) weighted by the density profile of the subject can be estimated. These receive profiles are independent of the transmit coil and transmit profile. Then the B1+ of the other modes or individual coils can be estimated by dividing the acquired image by the estimated received profile. Even though the long TR and acquisition time are required to measure B1+ and B1- of the birdcage mode, to estimate the B1+ of the other seven modes, only one image per mode is needed. For the other seven modes, the absolute amount of errors in the B1+ estimate due to noise is not amplified by the small B1+ and independent of the flip angle in the low flip angle regime as long as the SNR of the B1- estimate is large enough. Thus, this relative B1+ mapping method depends on the good estimate of B1- which requires only one good combined mode. This method is not the constrained by the condition number of the transform matrix in [39] or the small B1+ of eight combined modes.

For eight channel parallel transmit system, the butler matrix [12] distributes the power equally to each individual coil. Through the butler matrix, the birdcage mode is limited to 1/8 or less of the total power the system (RFPA) can drive. By using the Butler matrix, the maximum voltage of the RF pulse delivered to the transmit coils can be 35% of the voltage without the butler. If the transmit coil has a small B1+, the limited maximum voltage makes the duration of the RF pulse, saturation pulse, to be long to achieve a large flip angle. We can instead generate the birdcage or combined mode by applying eight RF pulse to the eight transmit coils.

In this work, we apply relative magnitude and phase B1+ mapping method to estimate the B1+ map of the eight TX channels. B1- map is estimated through a combined mode and the B1+ map of the eight TX channels are estimated by dividing the image of the individual coil by the B1- profile. At first we collect eight images with a low-flip-angle excitation for each individual coil

with a short TR (2s for in-vivo subject). Each image is acquired in a single TR using a turbo-flash sequence. The T1 effect is further diminished by acquiring the center of the k-space using the centric reordering of phase encoding lines. However, to reduce the filtering effect due to uneven longitudinal magnetization before excitation pulses in the turbo-flash readout, we apply very small flip angle less than 5~10 degree. Based on these images, we calculate a best combination that minimizes the ratio of the maximum to minimum intensity of the combined image inside region of interest (ROI). Unlike the standard birdcage mode, a fixed combination of the TX coils, this optimal combination depends on relative location of the subject to the TX coil and the ROI, and the optimal combination varies, especially for multi-slice acquisition.

To reduce the acquisition time to estimate the magnitude of B1+ and complex B1- of the synthesized combined mode, we apply the multi-saturation angle method [20, 46]. We acquire one reference image with a short TR (2s for in-vivo subject) and one or several saturation images with a long TR (20s for in-vivo subject) using a turbo-flash readout. For each voxel, the images are fitted to a cosine curve and we estimate the B1+ of the birdcage mode and the receive profiles.

We also take advantage of the spatially smooth nature of the |B1+| maps to reduce the acquisition time or increase the number of slices in one TR for multi-slice acquisition through the application of compressed-sensing reconstruction. This smoothness constraint holds true even though the underlying images have anatomic contrast independent of the coil maps. This smoothness can be used to increase the sensitivity of the B1+ estimate to noise [47]. The acquired images contain not only the B1+, but the density profile of the subject and the receive profiles. We propose a novel compressed sensing (CS) reconstruction method that imposes the sparsity of the flip angle image to reduce the acquisition time to measure the B1+ and B1- mapping of the combined mode. For CS reconstruction, only one fully-sampled reference image of the combined mode, which is very short, is measured to capture the complexity of the receive profile and the density profile, but the other images with the saturation pulse can be highly under-sampled. For saturation images, the TR is limited by the T1 relaxation effect and thus we

cannot decrease. However, with the CS approach, we can decrease the scan time for 2DFT readout or interleave more slices in one TR for turbo-flash readout so that the total acquisition time can be reduced for multi-slice acquisition of the whole brain.

2.2 Methods

2. 2.1 Fast B1+ mapping

Our approach is focusing on a method to get a good B1- estimate, and consists of six steps as follows:

1. Collect a low flip angle image per each individual transmit coil with the TR of 2s.

2. Find a best linear combination of individual coils that minimizes the ratio of the maximum to the minimum intensity of the combined mode.

3. Collect a reference (without saturation pulse) with the TR of 2s and saturation (with the saturation pulse) images on the combined mode with the TR of 20s with the low flip angle excitation used in the step 1.

4. Fit the intensity of the images into a cosine curve for each voxel and determine the magnitude B1+ of the combined mode.

5. Estimate the receive profiles, B1-.

6. By dividing out the receive profile from the eight low flip angle images collected in the step 1, estimate the B1+ of the eight individual transmit coils.

In the first step, we acquire the images from each individual coil with a low flip angle excitation in order to ignore or reduce the T1 relaxation effect even with a short TR (2s). These images are acquired in a short TR with a low flip sinc excitation pulse whose nominal flip angle is two degree in the standard birdcage mode and slice thickness 10 mm, the turbo-flash readout in centric reordering. With this low flip angle the longitudinal magnetization before the excitation pulse played is almost the same as the spin density. Each individual image has the same underlying receive profile. In the low flip angle regime, these images, I_k, form the basis of the images we can acquire from the pTx system. To estimate the B1-, we find a best combination of eight individual images that minimizes the dynamic range, the ratio of the maximum to the minimum intensity inside a chosen region of interest (ROI) such as brain. The favorable combination, determined by the relative amplitude and the phase, c_i, delivered to the individual transmit coils, which the parallel transmit system has a freedom of, can remove the region of very low flip angle excitation in the combined mode, decrease the sensitivity of the B1+ estimate to the noise, and decrease the dynamic range of the B1+ in the combined mode. The combined image can be written as

$$I_c(x,y) = \sum c_i I_i(x,y) = \sum c_i \rho(x,y) RX(x,y) \sin\left(\theta_i(x,y)\right),$$

where θ_i is the flip angle of transmit coil i, ρ is the spin density profile and RX is the sensitivity of the receive coils, and we call ρ RX the receive profiles. In the low flip angle regime, this can be approximated as (none of these terms are defined)

$$I_c(x,y) \cong \rho(x,y) RX(x,y) \sin\left(\sum c_i \theta_i\right).$$

We represent the coefficients as a column vector c whose entries are the conjugate of c_i and the intensity of eight images as a column vector Im(x,y) for each voxel (x,y). In the iterative process, we normalize the coefficients to fix their sum of squares to be one. In other words, the two-norm of the vector c is one. In a practical sense, we keep the total power delivered through the eight channel transmit coils. The minimizing criterion can be represented as

$$c = \arg\min_{\|c\|=1} \left\{ \max_{(x,y)\in ROI} \left| I_c(x,y) \right| / \min_{(x,y)\in ROI} \left| I_c(x,y) \right| \right\}$$
$$= \arg\min_{\|c\|=1} \left\{ \max_{(x,y)\in ROI} \left| c^H \, \mathrm{Im}(x,y) \right| / \min_{(x,y)\in ROI} \left| c^H \, \mathrm{Im}(x,y) \right| \right\}.$$

We have developed an iterative process to find the vector c. The standard birdcage combination is used as the initial coefficients. For each iterative step, instead of minimizing the ratio, we find the vector c that increases the minimum intensity and decreases the maximum intensity. For each iterative step, we calculate the intensity of the combined image. To increase the minimum intensity, the vector of the coefficients, c, is updated to increase the magnitude of the inner product between c and $\mathrm{Im}(x_{min},y_{min})$ at the voxel of the minimum intensity. This is done by adding a vector along the direction of the $\mathrm{Im}(x_{min},y_{min})$. To decrease the maximum intensity, we subtract a vector along the direction of the $\mathrm{Im}(x_{max},y_{max})$ at the voxel of the maximum intensity from the vector c. Then, we normalize the vector c and iterate the process. The two-norm of vectors added and subtracted to the vector c is initialized as 0.01 and decreased by a factor of 0.995 in each iterative step.

We estimate B1+ of the combined mode, and using this estimate, we determine the receive profile. For this step, our method accommodates the use of a variety of previously proposed B1+ mapping methods, such as the double-angle method [16, 19], multi-angle method [11, 17], saturation angle method [20, 46], and AFI [15]. In the current implementation, we used a multi-saturation angle method with the turbo-flash readout in centric reordering [20, 46, 48] due to its fast acquisition, one image per TR, and lower sensitivity to eddy currents and B0 inhomogeneity than Echo Planar Imaging (EPI). The same sinc excitation pulse, whose nominal flip angle is two degree and slice thickness 10 mm, used in the individual coils is used again for the combined mode. We have collected a reference image without the saturation pulse and several saturation images with the high flip varying saturation flip angle. For reference image, we have used a short TR (2s) but for the saturation image, we have used a long TR (20s) due to high flip saturation angle. With the low flip angle excitation, whose flip angle is two degree, the T1 relaxation effect can be ignored and the image can be estimated as

$$I_{ref}(x,y) = \rho(x,y)RX(x,y)\sin(\theta(x,y)),$$
$$I_{sat}(x,y,n) = \rho(x,y)RX(x,y)\sin(\theta(x,y))\cos(n\theta_s(x,y)),$$

where θ is the flip angle of the excitation pulse and θ_s is the flip angle of the saturation pulse delivered though the combined mode.

For each pixel, the images are fitted into the cosine curve of the saturation flip angle. By this fitting method, we can estimate the actual saturation angle, $\theta_{s,act}(x,y)$, and the multiplication of the density of the subject, the receive profile(B1-), and the sine of the excitation flip angle, $\rho(x,y)RX(x,y)\sin(\theta(x,y))$, can be estimated. The relative B1+ profile can be estimated as

$$B_1^+(x,y) = \theta_{s,act}(x,y) / \theta_{s,nor}.$$

Then we can determine the actual excitation flip angle

$$\theta_{act}(x,y) = B_1^+(x,y) \cdot \theta_{nor}.$$

By dividing the reference image out the sine of the actual excitation angle, we can estimate the multiplication of the density of the subject and the receive profile,

$$\rho(x,y)RX(x,y) = I_{ref}(x,y) / \sin\left(\theta_{act}(x,y)\right).$$

This receive profile is used in estimating the B1+ of the individual coils. The actual excitation flip angle is estimated by dividing the image by the multiplication of the density of the subject and the receive profile (B1-). Then, the B1+ profile can be estimated as

$$B_1^+(x,y) = \theta_{act}(x,y) / \theta_{nor}.$$

2.2.2 Validation

To demonstrate the utility of the proposed B1+ mapping method, we have designed the B1+ mitigated pTx RF pulses with B0 tracking and applied them to phantom and in-vivo experiments at 7T. We compared the flip angles measured by the scan to the flip angle estimated by the Bloch simulation using the measured B0 and B1+ map.

For low flip angle validation, we designed the two spokes for slice selective excitation [11]. The low-flip-angle pulse was played as an excitation pulse in a gradient-echo sequence for all eight channels. By diving out the receive profile, the excitation angle can be estimated. We applied this low flip angle pulse both for phantom and in-vivo experiments.

2.2.3 Compressed Sensing

We have applied compressed sensing (CS) approach on estimating B1+ and B1- profile through the combined mode. The B1+ map is much smoother than typical in vivo images collected from human subjects, which in addition to anatomic contrast, are influenced by spin density profiles, receive profiles, and transmit profiles. We impose the spatial smoothness constraints not on the individual image but on the B1+ map so that it has a sparse representation under finite difference, TV norm, transformation, which in turn can be used to regularize the reconstruction of these data from a limited set of samples. We impose the sparsifying transformation, total variation (TV) norm criterion, only inside an ROI, which for in-vivo data we chose as the entire brain within an axial section. We denote the Fourier transform followed by under-sampling as $F_{u,n}$, individual image as I_n, the under-sampled raw data as $d_{u,n}$. We estimate the magnitude of B1+ by minimizing the following CS criterion:

$$B_1^+ = \arg\min_{B_1^+} \sum \left\| F_{u,n}\{I_n\} - d_{u,n} \right\|_2^2 + \lambda \left\| B_1^+ \right\|_{TV,ROI}.$$

For the saturation angle method, we have developed a simpler approach that obtains the reference image, I_{ref}, with full Nyquist sampling to capture the complexity of density and receive profiles, highly-under-sampled data for the saturation images, I_{sat}. With these images we estimate the saturation flip angle, which will be used to estimate the B1+, by CS reconstruction. The CS criterion can be simplified as

$$\theta_s = \arg\min_{\theta_s} \left\| F_u\{I_{ref} \cos\theta_s\} - d_u \right\|_2^2 + \lambda \left\| \theta_s \right\|_{TV,ROI}.$$

As an initialization, we under-sample the reference image with the same sampling pattern applied in the saturation image. The ratio of the two under-sampled images determines a low-resolution estimate of the saturation flip angle. Then, we smooth the initial estimate and iterate the minimization process by the steepest-descent algorithm.

2.3 Experimental Result & Validation: In-vivo & Water Phantom Scans

2.3.1 B1+ mapping

To evaluate the performance of the B1+ mapping method in an 8-channel parallel transmit system at 7T, we scanned one healthy volunteer with informed consent. An 8-channel loop transmit coil and an 8-channel wrap-around receive coil [49] are used. For the in-vivo subject, we collected the B1+ map and B1- map of the iso-center slice with the thickness of 10 mm, FOV_{xy} of 240mm, and resolution of 128*128.

For each individual coil, we collected low flip angle images with turbo-flash readout in a centric reordering with the TE of 1.96ms, the echo spacing of 4.4 ms, and the TR of 2000 ms. The same

slice selective sinc excitation pulse with the slice thickness of 10mm, the nominal flip angle of two degree, the duration of 1.6 ms, and the time-bandwidth product of 4 is applied for each individual coil. Figure 5 shows the magnitude of the images from eight TX coils.

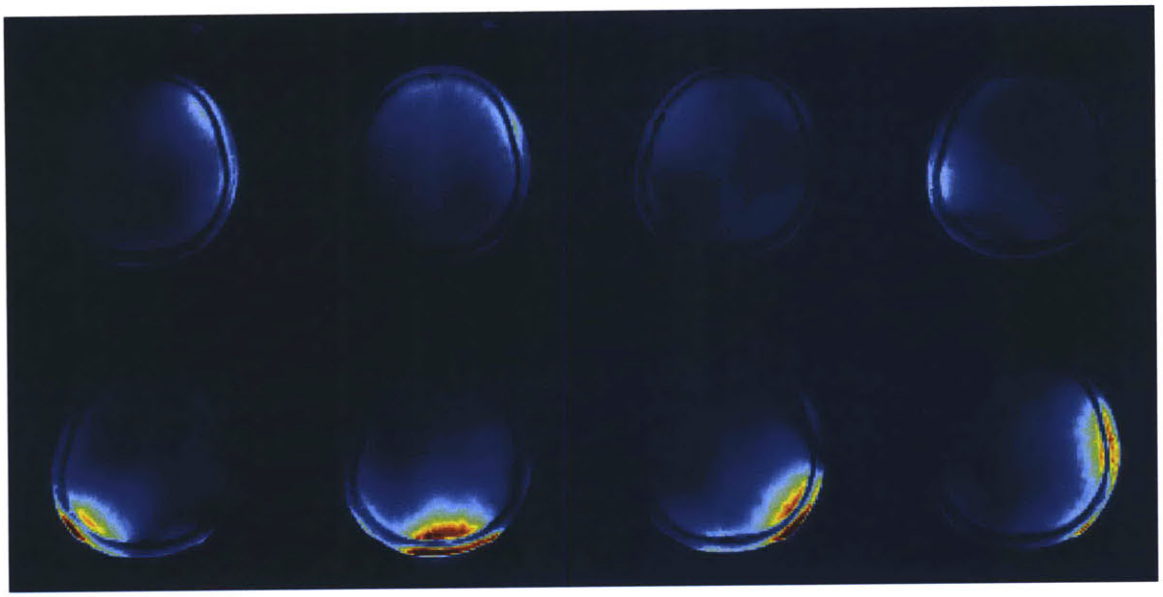

Figure 5: The magnitude of the low flip angle images from 8 TX coils

With these images we determine a combination to maximize the minimum intensity and minimize the maximum intensity of the combined image inside the brain. The iterations for 1,000 steps take a few second. Figure 6 shows the minimum intensity (a), the maximum to minimum ratio (b), the combined image inside the brain (c), and the image from the conventional birdcage mode (d) as a comparison. As shown in Figure 6, the iteration process converges to the minimum intensity of $1.3*10^{-5}$ and the maximum-to-minimum ratio of 2:1. The standard birdcage mode has the minimum intensity of $1.1*10^{-5}$ and the maximum-to-minimum ratio of 3:1.

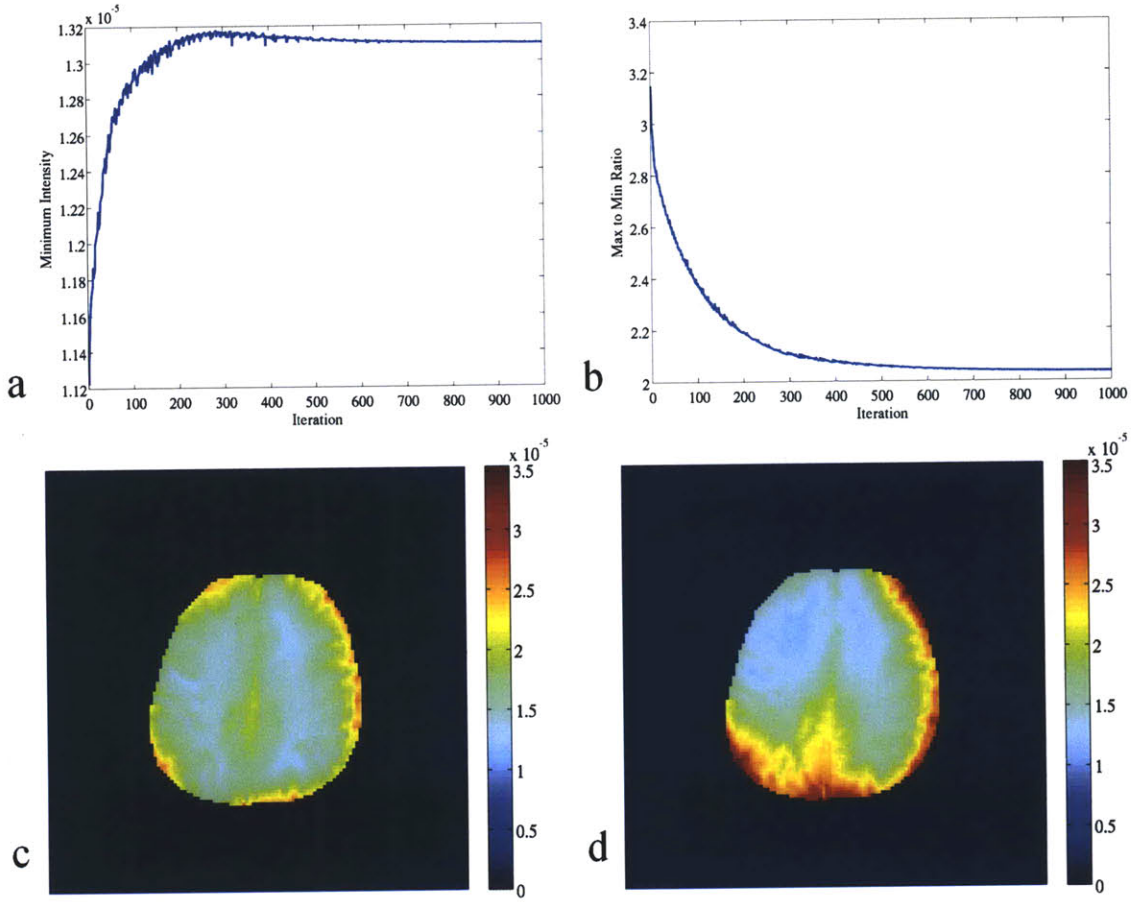

Figure 6: Combination of eight low flip angle images from the TX coils: (a) Minimum Intensity of the combined mode, (b) Maximum to Minimum ratio of the intensity in the combined mode, (c) Intensity of the optimally combined mode, (d) Intensity of the standard birdcage mode

Then, using this combined mode, we scan reference and saturation images to estimate the magnitude B1+ of the combined mode and finally the receive profile, $\rho(x,y)RX(x,y)$. The reference image is acquired in a short TR of 2s, but each saturation image is acquired in a long TR of 20s to remove the T1 relaxation effect. In this subject, we collected five saturation images. By fitting the intensity of the images for each voxel into a cosine curve, we estimate the saturation flip angle. To figure out the smallest number of saturation images we need, we also estimate the magnitude B1+ with a reference image and only one saturation image. Figure 7 shows the magnitude B1+ map inside the brain. The magnitude B1+ map with only one saturation image almost matches with the magnitude B1+ map with five saturation images with the RMSE of $3*10^{-6}$ G/V.

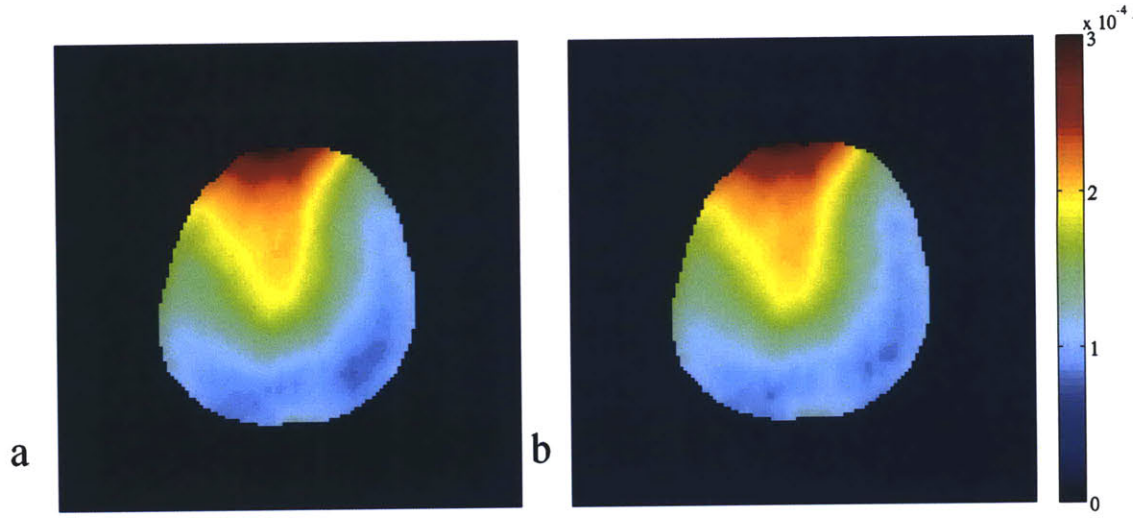

Figure 7: Magnitude B1+ map of the combined mode (G/V): (a) Estimated using one reference and five saturation images, (b) Estimated using one reference and one saturation image

With this B1+ map we can determine the flip angle of the excitation pulse. By dividing out the sine of the excitation flip angle from the reference image, we determine the receive profile, $\rho(x,y)RX(x,y)$ as shown in Figure 8.

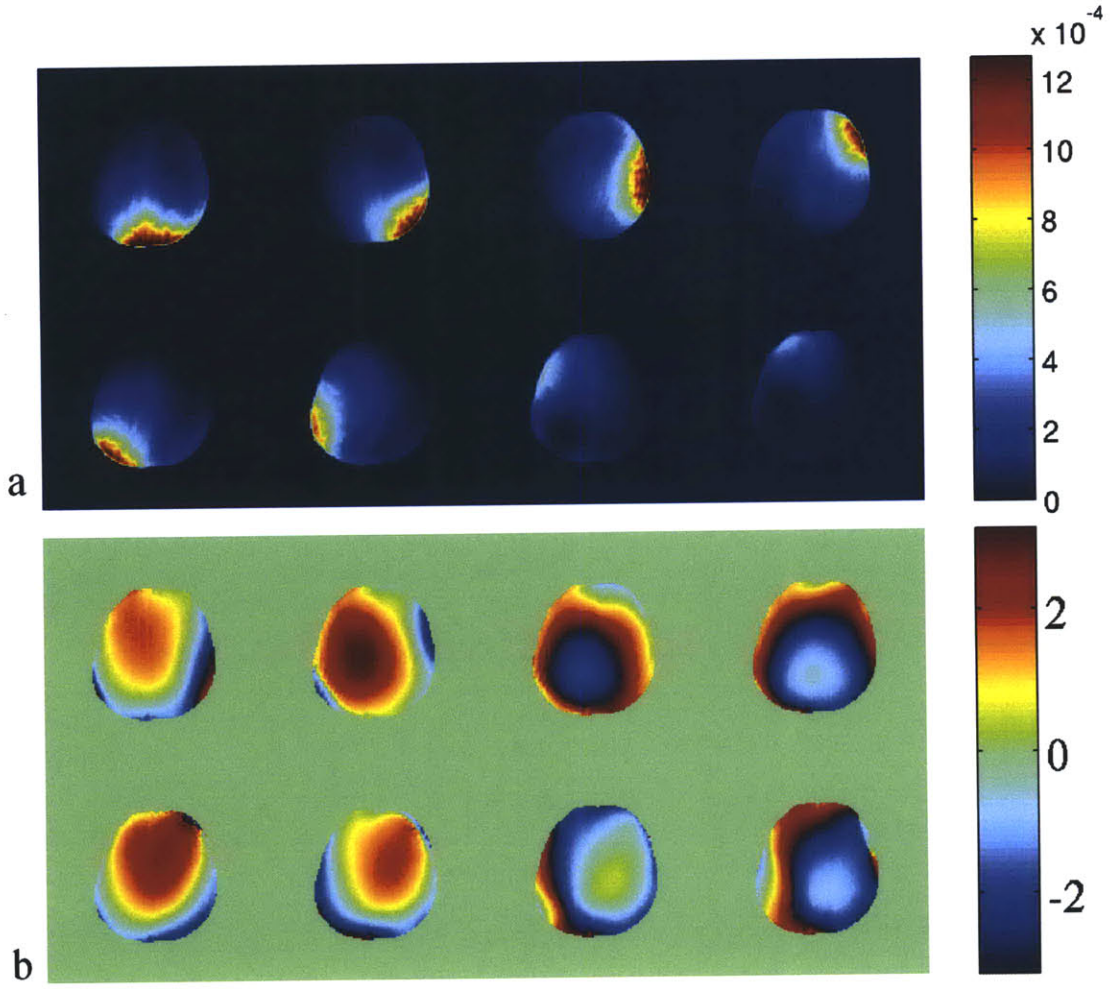

Figure 8: Receive Profile, $\rho(x,y)RX(x,y)$, of the wrap-around RX coil: (a) amplitude, (b) phase in radian

Finally, the B1+ map, or excitation flip angle, of the individual coil can be estimated by dividing out the receive profile from the low flip angle image acquired in the beginning of the whole process. The B1+ map in G/V is shown in Figure 9.

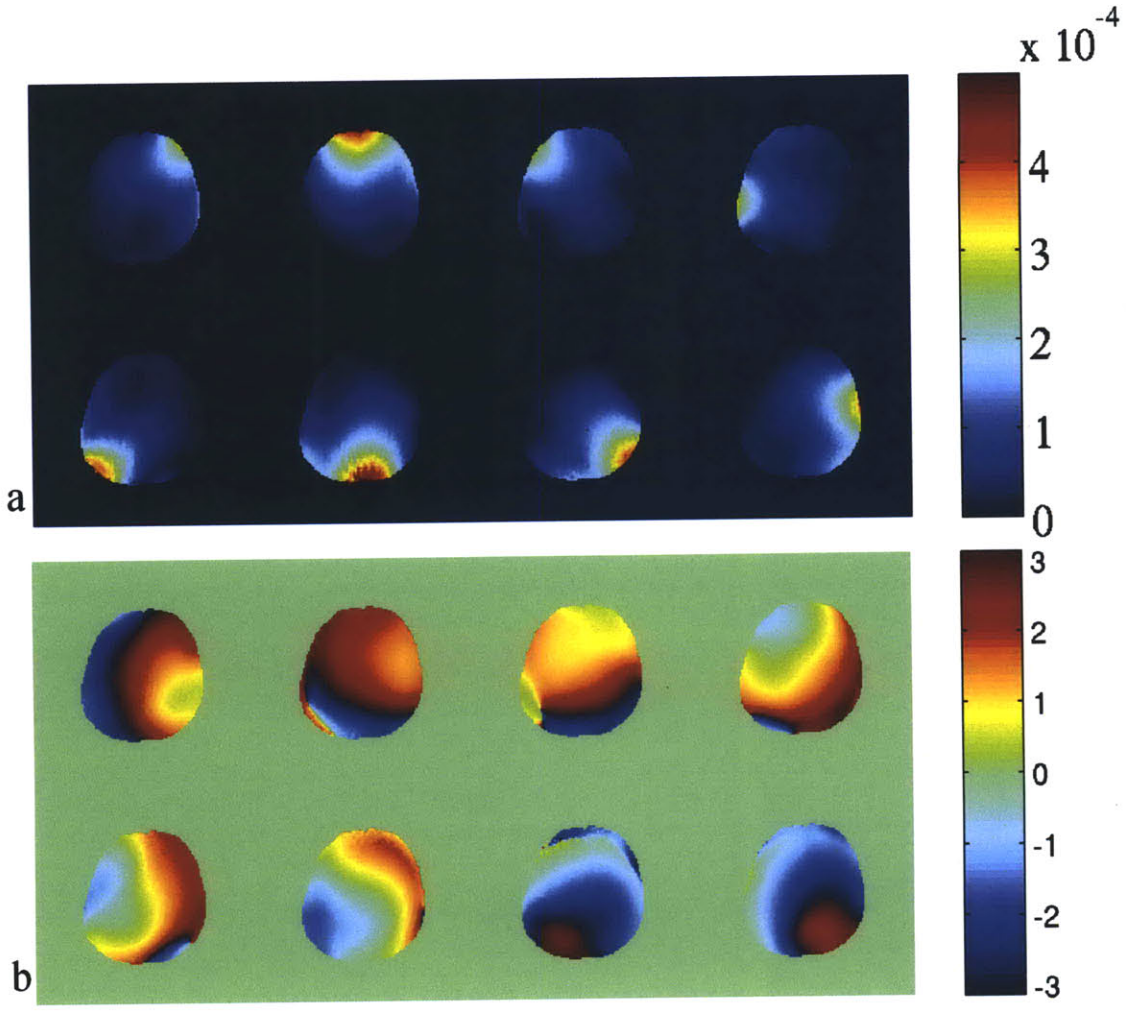

Figure 9: B1+ map of the 8 channel loop TX coil: (a) amplitude, (b) phase in radian

The entire scan takes 118 seconds, nine short TRs (2s) and five long TRs (20s). As it is shown in Figure 7, we can achieve almost the same performance with the RMSE of $3*10^{-6}$ G/V by acquiring one saturation image instead of five. In this single TR saturation image, the readout ends in 580 ms and thus we can use the TR of 580 ms for the saturation image with regard to B1+ mapping. The total scan time can be reduced to 19 seconds.

To validate the B1+ map estimate and to see the possibility of using this procedure for designing the slice selective ΔB0, B1+ mitigation pTx RF pulses, we have designed the MLS two spokes [11]. The RF pulse is designed for low flip angle regime and we scan with a gradient-echo

sequence whose TR is 100ms. By dividing out the receive profile from the acquired image, we estimate the transverse magnetization profile of the RF pulse. In Figure 10, we have shown the excitation flip angle from the Bloch simulation (a) and the measured (b). In the measured image, the T1 relaxation effect due to the short TR of 100ms is visible. The root mean square error (RMSE) between the Bloch simulation and the measured flip angle is 0.34 degree. The mean of the flip angle in the Bloch simulation is 5.77 degree.

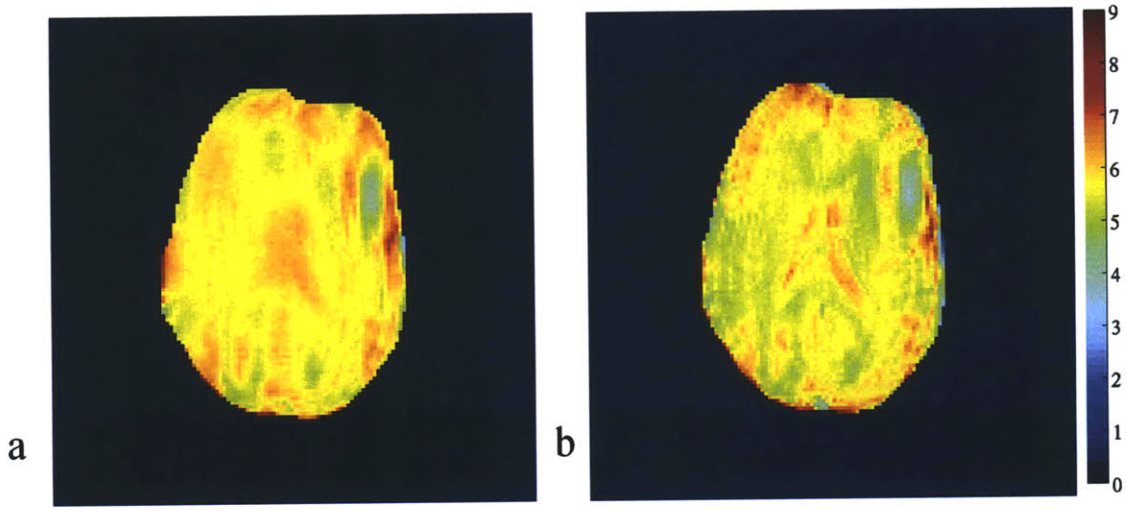

Figure 10: Flip angle (deg) of the MLS two spokes (*In-vivo*): (a) Bloch Simulation, (b) Measured

We scanned a head-shaped water phantom with the T1 of 175 ms. The specifications are the same as the in-vivo scan except TR of 1s for all turbo-flash scans and FOV_{xy} of 200mm. For validation, we designed the slice selective two spokes RF pulses. Figure 11 compares the measured flip angle to the Bloch simulation. The RMSE between the Bloch simulation and the measured flip angle is 0.18 degree for low flip angle shown in Figure 11(a-b). The mean of the flip angle in the Bloch simulation is 5.74 degree.

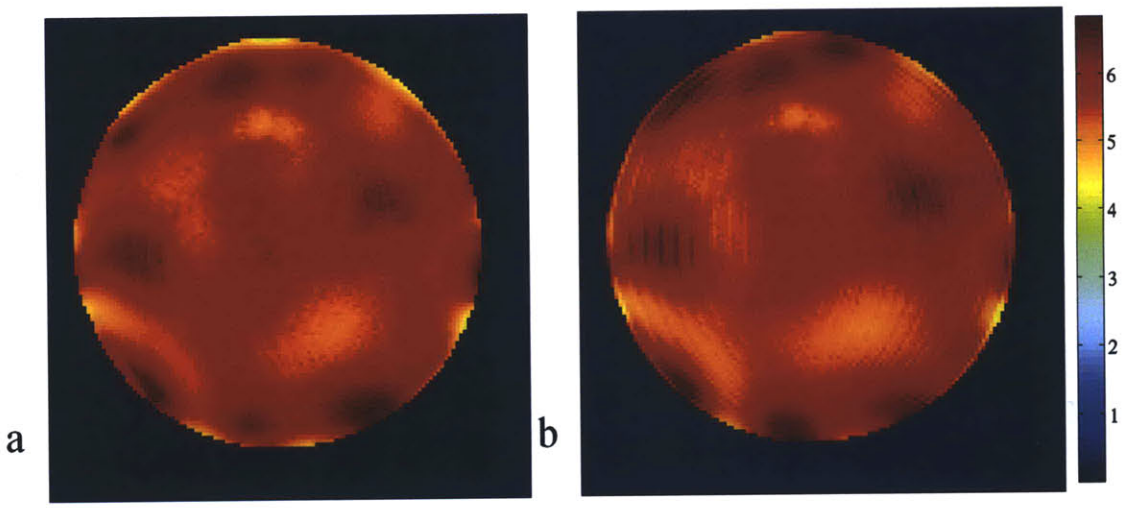

Figure 11: Flip angle (deg) in Water Phantom: (a) The Bloch Simulation for two spokes, (b) The measured for two spokes

These measured data for in-vivo and water phantom show the good match with the Bloch simulation. For the purpose of a slice-selective excitation by two spokes, our B1+ mapping approach fulfills the needs.

2.3.2 Compressed Sensing (CS)

To further reduce the scan time, we have applied CS approach for estimating the B1+ of the combined mode and the receive profile. We have tried CS reconstruction for one fully sampled reference image and one highly under-sampled saturation image. The B1+ map reconstructed by CS method is compared to the B1+ map estimated from the fully sampled image. To demonstrate the performance, we have simulated with the several under-sampling ratios. Figure 12 (b-e) shows saturation flip angle map of the combined mode in degree with 6, 10, 20, and 40 PE lines. Figure 12 (f) shows the RMSE of the saturation flip angle as a function of the number of PE lines. With 20 PE lines we can obtain a reasonable B1+ map.

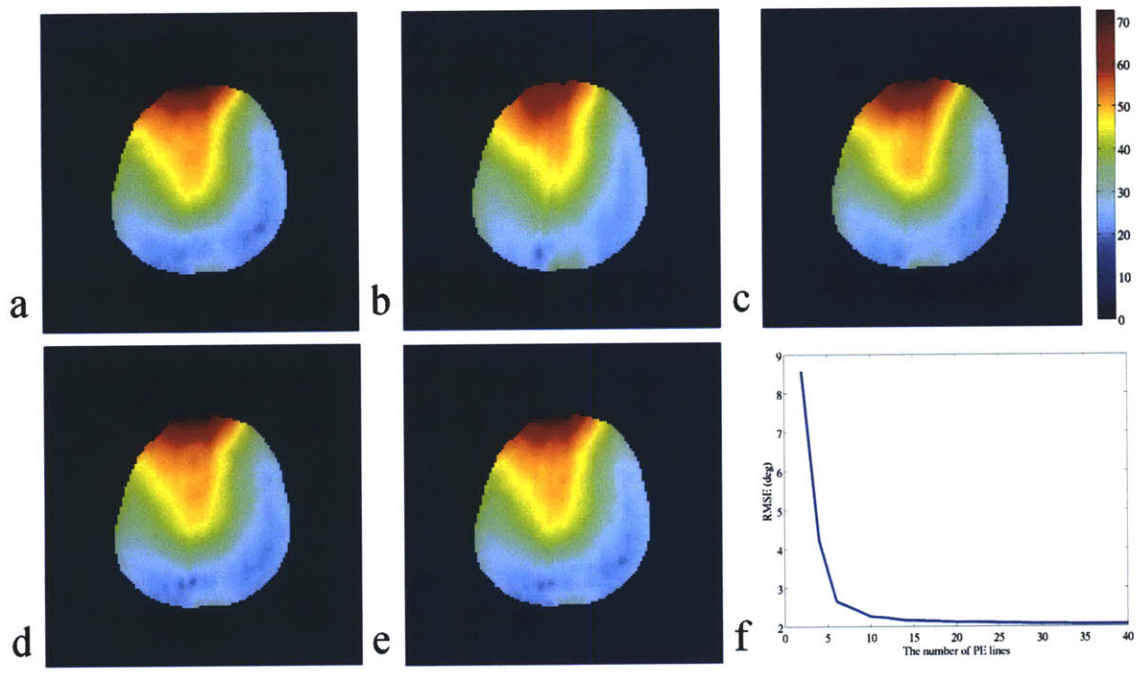

Figure 12: The performance of the CS method for estimating the saturation flip angle with highly under-sampled saturation image: Saturation angle map in degree with (a) 128 PE lines, (b) 6 PE lines, (c) 10 PE lines, (d) 20 PE lines, (e) 40 PE lines, and (f) The number of PE lines used in saturation image vs RMSE in the estimate of the saturation angle in deg.

2.4. Conclusion

We presented a B1+ mapping method for application in a parallel transmit system at 7T and demonstrated its use on phantoms and on human subjects. Our method addresses a critical challenge faced at high field for mapping of excitation and readout fields, which is the large dynamic range of the acquired data and consequent noise amplification in field estimation. In our method, the dynamic range of the data that enter the field estimation is dramatically reduced by optimally combining the eight images collected by the eight individual coils. The coefficients are calculated in real time and they depend on the relative location of the subject to the coil and the region of interest. We can acquire B1+ maps of the eight channel loop TX coil at 7T within 20 seconds for single slice, 29 seconds for five slices, 58 seconds for ten slices, and 116 seconds for twenty slices. We have validated the B1+ mapping method by two spoke design for low flip angle excitation. The mean of the flip angle inside the ROI and the RMSE between the Bloch

simulation and the measured flip angle are 5.77 degree, 0.34 degree for in-vivo and 5.74 degree, 0.18 degree for phantom. The scan time can be further reduced by a novel compressed sensing method that imposes the smoothness (sparsity) of the B1+ map. With 20 PE lines we can obtain a reasonable B1+ map.

For multi-slice acquisition, we can compute the best combination of individual images in each slice, and the coefficients of the best combination will not be the same. To reduce the scan time, multi-slice acquisition can be interleaved. With the resolution of 128*128 the scan takes 29 seconds for five slices, 58 seconds for ten slices, and 116 seconds for twenty slices. With the resolution of 64*64 the scan takes 19 seconds for five slices, 29 seconds for ten slices, and 57 seconds for twenty slices.

Chapter 3

Local-SAR Constrained RF Design for Parallel Transmission

3.1 Introduction

Recent work has demonstrated great utility of parallel transmission (pTx) systems for radio frequency (RF) pulses in magnetic resonance imaging (MRI) for the purpose of generating much more flexible magnetization profiles than is feasible with conventional single-channel RF systems [8-13].

A critical challenge in pTx RF design is the minimization of specific absorption rate (SAR), which is a measure of the deposited power per unit weight of tissue due to the RF pulse. Maximum values for SAR are specified by safety regulations and must be met both globally (e.g. power absorbed by the whole head or whole body) and locally (e.g. power absorbed per 10 grams of tissue). While global or average SAR values are readily measured and easily amenable to incorporation as constraints in the pTx RF pulse design, brute-force local SAR minimization during the design of pTx RF pulses poses a challenging optimization problem with a heavy computational burden.

In this work, we describe and demonstrate a method for pTx RF design that efficiently incorporates local SAR constraints RF pulse design for in parallel transmission. The proposed method applies recently introduced model compression method for local SAR estimation [42] to dramatically decrease the complexity of the prediction of the peak local SAR. Due to this model compression method, the spatial distribution and maximum magnitude of local SAR values can be represented with dramatically reduced model complexity. For instance, in a discretized human numerical model of human tissue types (electric conductivity σ, permittivity ε, density ρ) typically used for field and SAR simulations with ~10^5 voxels can be compressed to as a few hundred so-called Virtual Observation Points (VOP). Representing the local SAR distribution via these VOPs, it becomes feasible to incorporate local SAR constraints in pTx RF design, which is subject of the description below.

We integrate VOPs into previously proposed iterative pTx pulse design methods by approximating the peak 10g local SAR as the weighed sum of the 10g local SAR in the complexity-reduced model. In each iterative step, we update weighting factors to achieve a better approximation of the maximum local SAR. This approach can be applied to several proposed pTx pulse design methods such as RF shimming [50], spatial domain design for small flip angle approximation [51], magnitude least squares (MLS) spoke design [13], arbitrary excitation for spiral trajectory [8], and composite pTx pulse for uniform volume excitation [44].

Compared to previous pTx designs with only an average SAR constraint, with the local-SAR-constrained design we demonstrate a decrease in peak 10g local SAR by 20-40%. This reduction in local SAR is important for pTx applications, and demonstrates that for a fixed RF pulse design performance (as measured by its ability to modulate the spatial flip angle), the proposed method holds the potential to reduce local SAR while enabling fast pTx RF pulse design.

3.2 Methods

3.2.1 Local SAR calculation

We apply an FDTD (Finite Difference Time Domain method [52]) numerical simulation of electrical and magnetic fields in a segmented tissue to estimate local and global SAR due to RF pulses played on an pTx coil array.

As an input, a unit signal, the RF pulse of one volt for 10μs duration, is played for each individual coil, k, in the array and the resulting electric, E_k, and magnetic, B_k, fields for x, y, z directions are stored. Then, for any instantaneous (10μs duration) pTx RF pulse, b, the electrical field at a voxel v can be calculated as $E_v = Q_v b$, where the k^{th} column of Q_v is the pre-calculated electrical field, E_k, in voxel *v*. The number of entries in the row vector E_v is three corresponding to x, y, z direction, the dimension of matrix Q_v is three (x, y, z direction) by the number of transmit coils, the number of entries in the column vector b is the number of transmit coils.

With the density, ρ (Kg/m^3), and the electric conductivity, σ (S/m), of the head model, local SAR at a voxel v can be determined as it is described in [53] by

$$SAR_v = \sum_t SAR_v(t) = \sum_t \frac{\sigma_v}{2\rho_v} \|E_v(t)\|^2 = \sum_t b(t)' S_v b(t), \text{ where } S_v = \frac{\sigma_v}{2\rho_v} Q_v' Q_v .$$

The regulatory limits on local SAR are specified for 10-g tissue volumes. For a 10-gram SAR calculation, we pre-calculate the 10-gram region around the voxel v, v_{10g}, and average the SAR in the region,

$$SAR_{v,10g} = \frac{\sum_{w \in v_{10g}} SAR_w}{|v_{10g}|} = \sum_t b(t)' \left(\frac{\sum_{w \in v_{10g}} S_w}{|v_{10g}|} \right) b(t) = \sum_t b(t)' S_{v,10g} b(t). \qquad \text{(Eq. 1)}$$

3.2.2 Model Compression Method for Local SAR estimation

The model compression method recently proposed by Gebhardt et al [42], can reduce the complexity of the maximum local SAR calculation from having to evaluate Eq. 1 or every voxel in the model (~10^5) to only the VOPs (in our case, ~10^2). An exhaustive search of the maximum local SAR over the full set of model voxels with the eight core CPU system currently takes several minutes. For the compressed model of a few hundred virtual observation points, the maximum local SAR can be calculated within an order of 10 ms, which makes it feasible for integration into fast iterative pTx pulse design method that requires calculating the maximum local SAR for each iterative step. For example, in our proposed iterative method, we iterate ten times which corresponds to more than half an hour for exhaustive search but less than a second for SAR calculation over the complexity-reduced model. In the following, we summarize the idea behind the model compression method by Gebhardt et al [42]:

If the maximum local SAR of all the voxels is upper-bounded by the maximum local SAR of clusters which we call virtual observation points, A_j,

$$\max_v \sum_t b(t)' S_{v,Ngram} b(t) \le \max_j \sum_t b(t)' A_j b(t),$$

we need to consider the maximum local SAR on the clusters to monitor the maximum local SAR of the entire model. This inequality holds when for any voxel v, there exists a virtual observation point A_k such that $A_k - S_{v,10g}$ is a positive semi-definite matrix. By decreasing the number of clusters, the complexity of the maximum local SAR calculation is reduced, but the upper-bound of the maximum local SAR becomes looser.

3.2.3 Heuristic greedy algorithm for model compression

We have developed a heuristic greedy algorithm to find the VOPs as follows:

1. Choose an overestimation factor $\varepsilon > 0$.
2. In the j^{th} iteration, find the un-clustered voxel v such that the matrix $S_{v,Ngram}$ has the largest eigenvalue. This voxel v can have the maximum local SAR deposition among the un-clustered voxels. This voxel v is called dominating hot voxel (HV) of cluster C_j. We choose the matrix with the virtual observation point: $A_j = S_{v,Ngram} + \varepsilon I$.
3. Find all un-clustered voxels whose SAR matrix is upper-bounded by the virtual observation point, A_j, and place them in the cluster j.
4. Iterate over steps 2 and 3 until all voxels are clustered.

The overestimating factor, ε, trades off the complexity of the design and the tightness of the upper-bound of the maximum local SAR estimation. By decreasing ε , the approximation of the maximum local SAR is more accurate but the number of clusters is increased.

In the proposed method for pTx pulse design with efficient incorporation of local SAR constraints, we approximate the maximum local SAR estimate of the entire model as its upper bound, the maximum local SAR at the virtual observation points: $\max_j \sum_t b(t)' A_j b(t)$. If the upper bound is tighter and thus the approximation of the maximum local SAR estimate is more correct, the constraint of our pTx pulse design method is closer to the maximum local SAR of the all the voxels in the human (head) model. By increasing the number of clusters the upper bound can be tighter, but the complexity of the pTx design is increased.

3.2.4 Pulse Design Method

By the model compression method, the dominant local SAR regions are captured by the virtual observation points. By the heuristic approach, the maximum local SAR of VOPs can be represented as the sum of the maximum local SAR of the dominant hot voxels (HV) and overestimating term, which can be represented as a global power of the pTx RF pulses:

$$\max_{v\in 3D}\left\{\sum_t b(t)'S_{v,Ngram}b(t)\right\} \le \max_{v\in HV}\left\{\sum_t b(t)'(S_{v,Ngram}+\varepsilon I)b(t)\right\}$$
$$= \max_{v\in HV}\left\{\sum_t b(t)'S_{v,Ngram}b(t)\right\} + \varepsilon\sum_t |b(t)|^2.$$

Our pTx pulse design criterion minimizes the difference between the desired transverse magnetization, m_d, and the transverse magnetization, m(b), generated by the pTx pulse, b(t), with the additional constraints on the maximum local SAR. In the several previously proposed pTx pulse designs, SAR is regularized by the global power constraints:

Conventional (Global Power) method finds the pTx RF pulse, b(t), that minimizes

$$\|m_d - m(b)\|_2^2 + \lambda\sum_t |b(t)|^2,$$

whereas for the proposed method, with incorporation of local-SAR minimization via the VOPs, the constraints are represented as

the proposed method finds the pTx RF pulse, b(t), that minimizes

$$\|m_d - m(b)\|_2^2 + \lambda\max_{v\in HV}\left\{\sum_t b(t)'S_{v,Ngram}b(t)\right\} + \lambda\varepsilon\sum_t |b(t)|^2.$$

For both pulse design methods, the RF pulses are designed for a set of regularization parameter, λ, to illustrate the trade-off between RMSE and the global power constraints or peak 10g local SAR constraints. The overestimating factor, ε, is a tuning parameter that determines the relative contributions of the maximum local SAR of the dominating hot voxels and the global power. By decreasing ε , the complexity (the number of clusters) is increased but the contributions of the global power in the design are decreased.

We have developed the iterative pulse design process. In each iterative step, we approximate the maximum local SAR as a weighted sum of the local SARs in the dominating hot voxels:

$$\max_{v\in HV}\left\{\sum_t b(t)'S_{v,Ngram}b(t)\right\}+\varepsilon\sum_t|b(t)|^2 \cong \sum_t b(t)'\left(\varepsilon I+\sum_{v\in HV} w_v S_{v,Ngram}\right)b(t), \qquad \text{(Eq. 2)}$$

where w_v are the weighting factors. This approximation converts the maximum norm constraint to the weighted two norm (global power) constraint, which is feasible in many pTx pulse design methods [8, 13, 44, 50, 51]. For the initialization of the iteration, we choose the equal weighting factors with the sum of one: $w_v = 1/|HV|$. In each iterative process, we design the RF pulse that minimizes the weighted global power constraint. With the RF pulse designed, we calculate the local SAR over the dominating hot voxels. Then, we update the weighting factors based on the calculated local SAR to achieve a better approximation of the maximum local SAR in Eq. 2. We stopped the process after iterating ten times. The computation time for calculating the peak 10g local SAR over the VOPs ($\sim 10^2$) is negligible compared to the time to design the pulse. The computation time for the proposed pulse design method is about ten times of the conventional (Global power) method.

3.2.5 Simulation Method

The electrical fields and magnetic fields on the virtual family model [54] for an eight-channel loop coil in the pTx head system at 7T (298 MHz) were estimated by FDTD simulation. We include the head and the shoulder of the virtual family model shown in Figure 13 in the simulation with the voxel size of 3mm*3mm*3mm, the field of view of 62×44×47 cm^3, and the number of voxels in the brain and shoulder of 271,950. With the electrical field from the simulation, the conductivity and density profile of the model, and pre-calculated 10-gram region, we calculate the matrix, $S_{v,10g}$, in eq. 1 for all the voxels in the model.

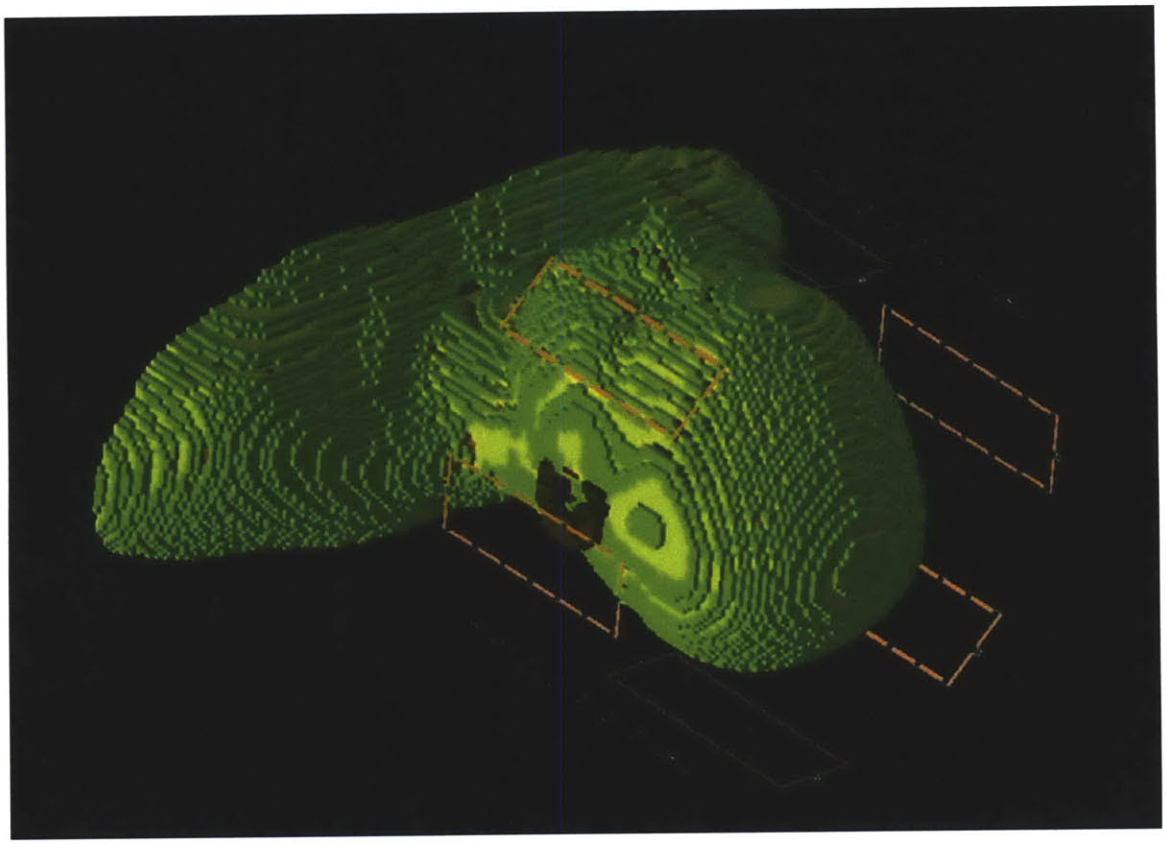

Figure 53: Shaded-surface rendition of the 3D digital head model (Ella model in the virtual Family and eight channel loop coil.

We have performed the model compression method of the maximum local SAR estimation with several overestimating factors. Figure 14 shows the number of clusters as a function of an overestimating factor. We chose 80 clusters (the point inside the oval) to cover the entire voxels in the model. In other words, our pTx pulses are designed with the local SAR constraint approximated by 80 VOPs. The SAR estimation by calculating the peak local SAR over 80 VOPs takes less than one second for ten iterations.

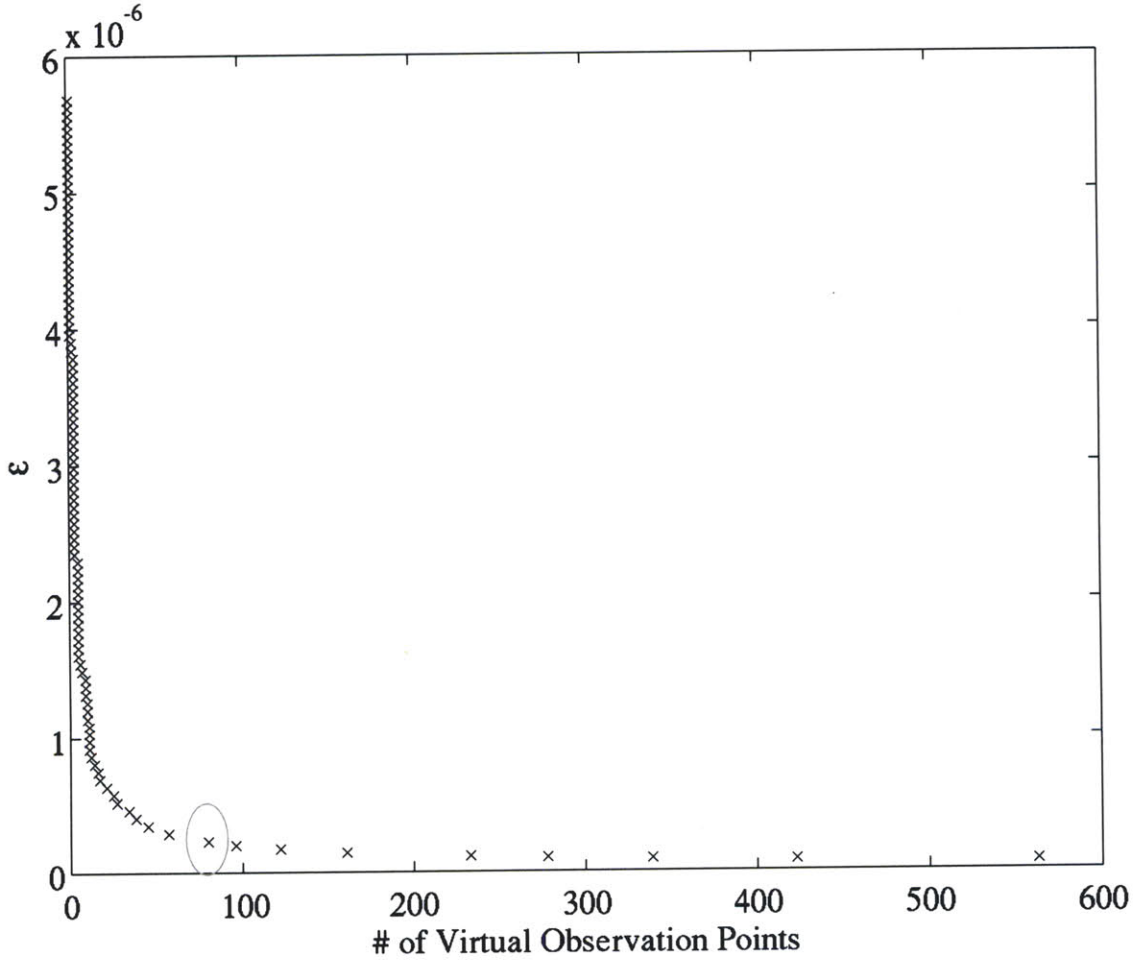

Figure 14: The number of clusters vs overestimating factor. We chose 80 clusters (point in the oval) for our pTx RF design.

3.3 Results

We demonstrate the application of the local SAR reduction in pTx design, by designing pTx pulses to mitigate magnitude of the B1+ inhomogeneity. The B1+ fields are simulated by the FDTD simulation, but we assume the B0 inhomogeneity is zero. We have designed two pTx pulses: (1) a two-spoke MLS pulse [13] for slice-selective excitation at iso-center (z=0) with a slice thickness of 10mm, and (2) a 2D spiral pTx pulse [8] with an acceleration factor of four with the MIT logo as a target pattern. The desired profiles are chosen to have the maximum transverse magnetization of 0.1 assuming that the fully relaxed longitudinal magnetization is one and shown in Figure 15.

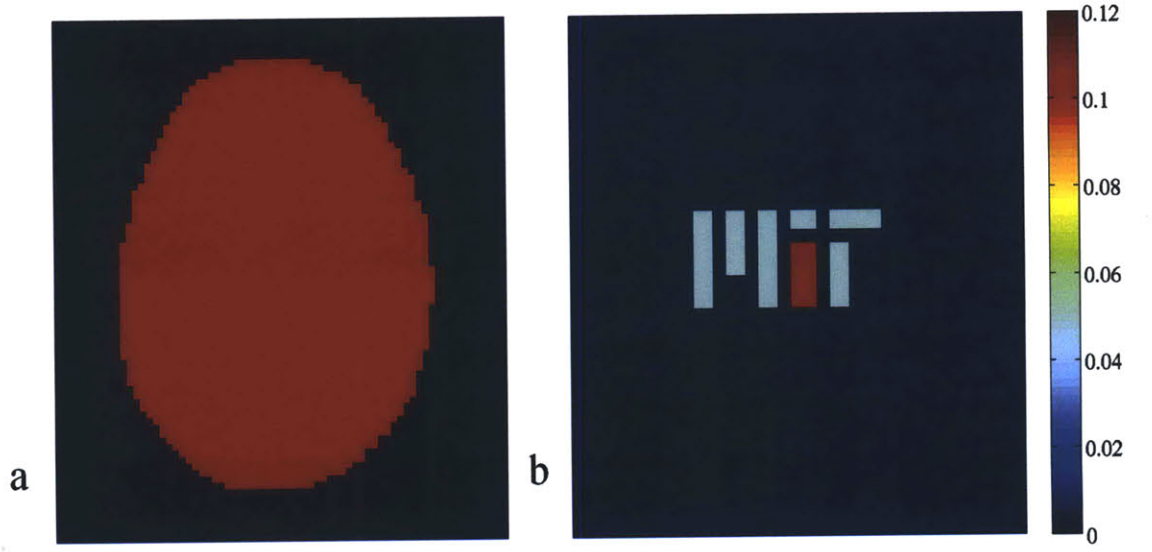

Figure 15: Target profiles, Mxy, for (a) MLS spokes for B0 and B1+ mitigation for slice selective excitation (b) spiral pTx pulse for Arbitrary Excitation (MIT logo)

We compared the local-SAR minimization performance of the proposed design, to conventional MLS spoke and 2D spiral pTx pulses, which includes only a global power constraint: $\left\|m_d - |m(b)|\right\|_2^2 + \lambda_1 \sum_t |b(t)|^2$. In both cases, we have calculated RMSE between the desired transverse magnetization profile, m_d, and the magnitude of the simulated transverse magnetization, ms, which is equal to |m(b)|, over the region of interest, brain, in the iso-center slice. RMSE can be written as

$$RMSE = \left(\sum_{x,y \in ROI} \left\| m_d(x,y) - m_s(x,y) \right\|_2^2 / |ROI| \right)^{1/2}.$$

We also calculated the peak 10g local SAR over the entire model by performing the exhaustive search for several λ , λ_1 . Figure 16 (a) shows the RMSE vs. peak 10g local SAR for both conventional and local SAR constrained two spoke designs. Compared to conventional design, our design can reduce the peak 10g local SAR by about 30%. Figure 16(b) and (c) demonstrates the transverse magnetization profile corresponding to the 29% reduction in peak 10g local SAR (RMSE = 0.0057) has a good magnitude B1+ mitigation for in vivo applications.

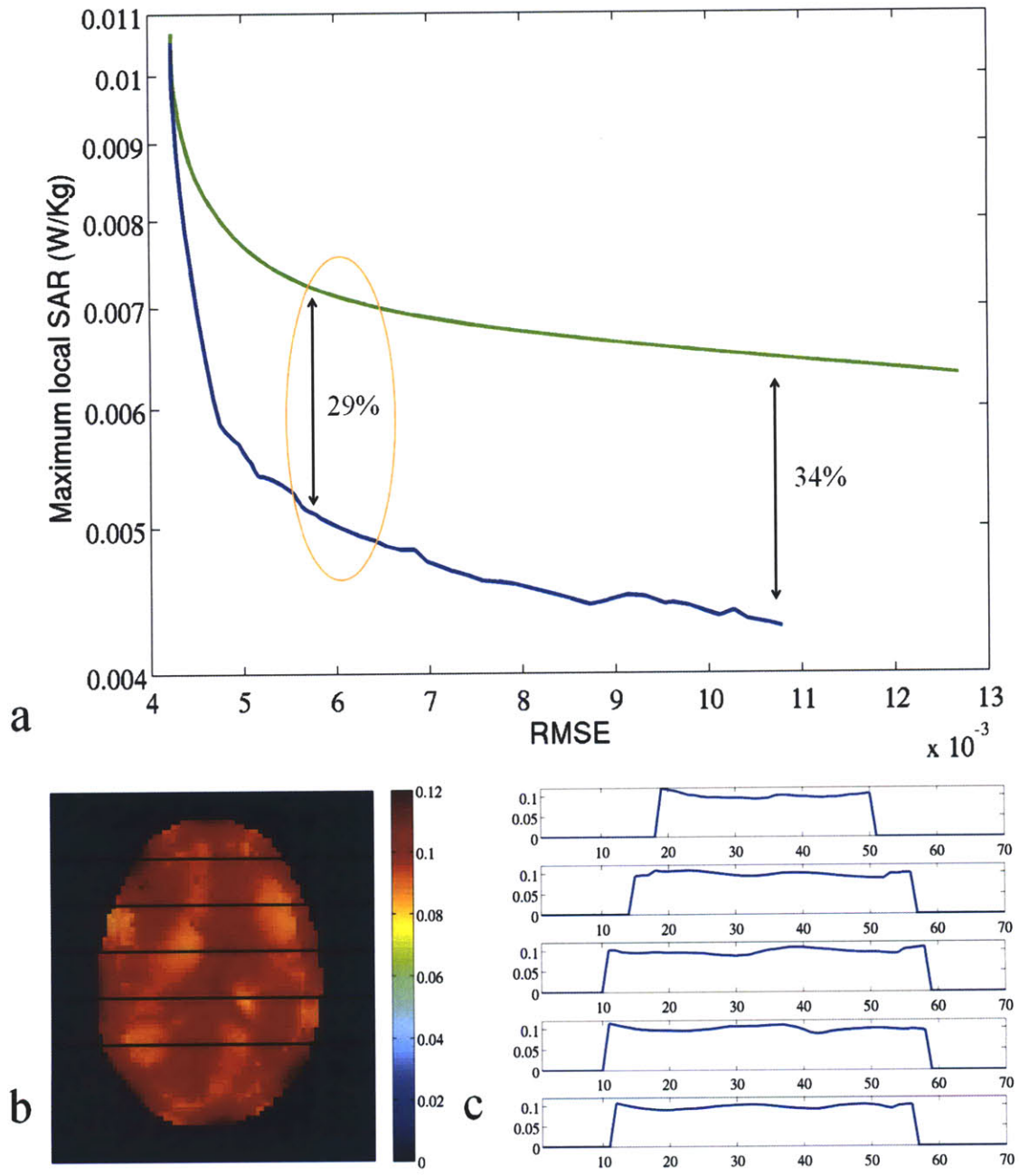

Figure 16: RMSE, the maximum local SAR and transverse magnetization for the two spoke design: (a) Root mean square error vs. Maximum local SAR for B1+ mitigation Green: Conventional, Blue: Proposed, (b) Tranverse magnetization (Mxy profile) corresponding to the orange oval in (a), (c) Transverse magnetization on the five black lines in (b)

Figure 17 shows the 10g local SAR maps, the Sagittal, Coronal, and Axial Slices containing the voxel with the peak 10g local SAR in the entire model (hottest voxel) of the two spoke design

corresponding to the 29% gap (RMSE = 0.0057) for are shown. Compared to the conventional method, the maximum local SAR is decreased by 29% and the hottest voxel slightly (15 mm Posterior, 18 mm Right, 6mm Foot) moved in the proposed method.

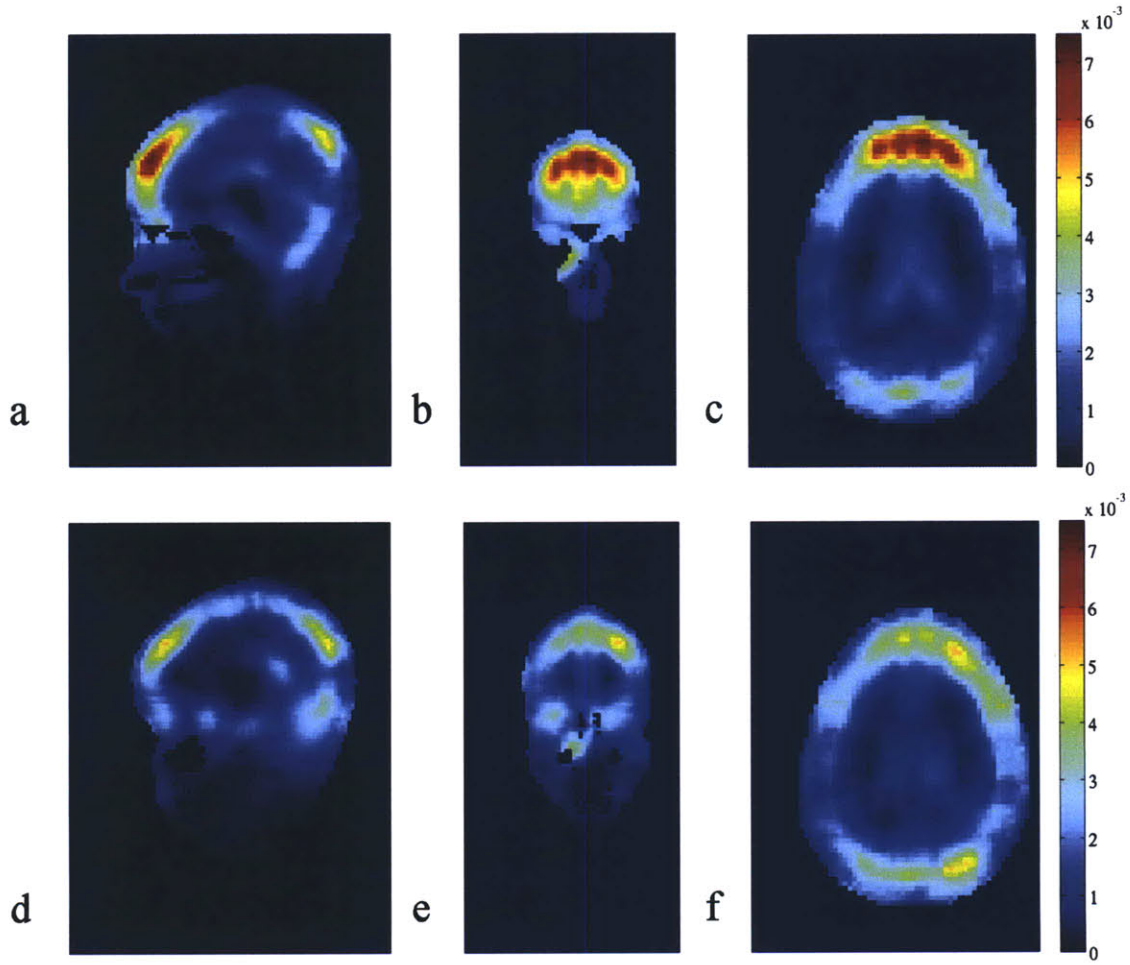

Figure 17: 10g Local SAR maps (W/Kg) of two spokes design for the orange oval in Figure 16(a): (a-c) Conventional, (a) Sagittal, (b) Coronal, (c) Axial, (d-f) Proposed, (d) Sagittal, (e) Coronal, (f) Axial

In Figure 18, we have shown the performance for the arbitrary excitation with spiral pTx pulse. The proposed method achieves 20~40% reduction of the peak 10g local SAR compared to the conventional design.

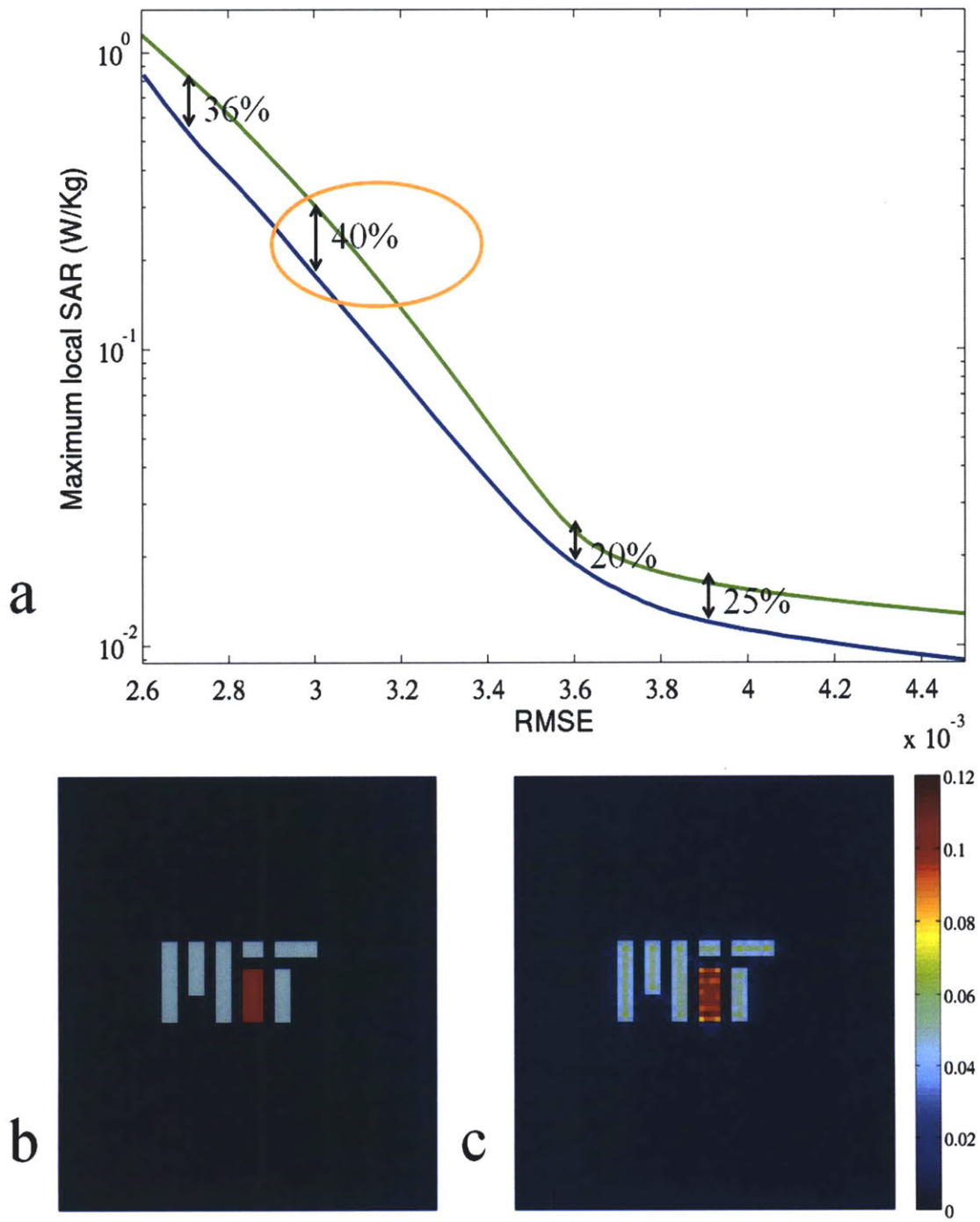

Figure 18: RMSE, the maximum local SAR and transverse magnetization for the two spoke design: (a) Root mean square error vs Maximum local SAR for MIT logo Excitation Green: Conventional, Blue: Proposed, (b) Target Profile, (c) Transverse Magnetization corresponding to the orange oval in (a)

3.4 Conclusions

We have developed an iterative pTx pulse design method that regularizes the maximum local 10g SAR of the entire set of voxels in a numerical human head model. The model compression method for the maximum local SAR estimate reduces the number of computed voxels by a factor of 3000, compared to an exhaustive search. This model compression method makes feasible the incorporation of local SAR constraints in the described pTx RF design. This design method is compatible with several pTx pulse design methods such as RF shimming, spatial domain design for small flip angle approximation, magnitude least squares (MLS) spoke design, arbitrary excitation for spiral trajectory, and composite pTx pulse for uniform volume excitation [8, 13, 44, 50, 51]. We have demonstrated about 30% reduction of the peak local 10g SAR with the proposed method compared to existing global power constrained designs for slice selective excitation with two MLS spokes and arbitrary excitation with spiral pTx pulse.

Chapter 4

Subcutaneous Lipid Suppression for Magnetic Resonance Spectroscopic Brain Imaging via Variable-Density Spiral Sampling, Real Time Filter Design, and Iterative Reconstruction

4. 1 INTRODUCTION

For brain magnetic resonance spectroscopic imaging (MRSI), estimates of brain metabolites using chemical shift imaging are severely hampered by strong lipid signals even though the interfering signal arises from regions outside of the brain, namely subcutaneous tissue, scalp, and bone marrow. Membrane lipids within the brain are not visible at intermediate and long echo time (TE) due to their short relaxation times [1]. Since SNR in MRI is proportional to voxel size [6], the low metabolite concentration, and consequently low SNR in spectroscopic imaging, dictates relatively large voxel sizes for reliable spectroscopic signal detection and quantification. The combination of a large voxel size and much higher concentration of lipids than proton brain metabolites (the ratio of peak lipid spectra to peak NAA spectra is about 100 at TE = 144 ms and TR = 2000), leads to the side lobes in the spatial impulse response as a significant contributor to

interfering and undesired fat signals in spectra within the brain. This problem is all the more challenging due to the spatial proximity of the cortex to the source of the undesired signals, as well as the narrow spectral separation between lipids components in the 0.9-1.3 ppm range and the dominant NAA resonance at 2.0 ppm, which corresponds to a minimum separation of 86 Hz at 3T. The spectral peaks of NAA and nearby lipids overlap due to line-broadening from T2 and T2* as well as chemical shift due to B0 inhomogeneity.

Several different methods of lipid suppression, including outer-volume suppression (OVS) [55-58] inversion-recovery [59-61], selectively exciting brain-only (PRESS [62], STEAM, Spectral-Spatial Excitation [63]), have been proposed and applied. These methods provide effective lipid suppression but inevitably trade off some amount of brain metabolite signals. At high field strengths (7T), spectrally-selective lipid-inversion has been proposed [64] to minimize any detrimental impact on metabolite signals while still achieving robust lipid suppression through inversion recovery.

An alternate approach for lipid suppression in brain CSI is based on methods to reduce the magnitude of spatial side lobes in the spatial impulse response and relies on the spatial separation between the brain and skull. To implement this idea, variable-density spiral trajectories have been proposed that collect outer regions in k-space along with properly matched filtering to localize lipid signals spatially to reduce the amount of spatial signal leakage without SNR tradeoffs as demonstrated for imaging [65] and spectroscopic imaging [43]. To rely on variable-density spiral sampling as the sole means of lipid suppression places substantial requirements on filter design (at least 30 dB suppression over a 5mm wide transition band for TE = 144ms) and image reconstruction to achieve the required stringent transition-band and stop-band characteristics as well as the gradient hardware system and careful attention to the k-space trajectory.

Prior work on variable-density sampling in MRSI [43] relied on a simple 1-D filter design (Hanning filter). While the methods presented in the current work are general, a particular motivation for our work is the effective suppression of in-brain lipid signals from adjacent, undesirable, and strong subcutaneous lipids by the means of variable-density k-space sampling to

achieve an isotropic spatial impulse response. We present an algorithm for the direct design of an optimal, spherically symmetric spatial filter in two or three dimensions to minimize lipid contamination while maintaining optimal SNR for brain metabolites. With the aid of quickly-acquired prior data, i.e. an image of the lipid sources, we design an acquisition-specific filter that not only has the desired voxel size to support the required metabolite SNR, but also provides sufficient spatial decay of the spatial side lobes of the impulse response to suppress lipid artifacts throughout the brain, including the cortex.

The SNR is optimized under matched filter conditions, i.e. when the density of the k-space sampling trajectory is proportional to the filter coefficients [6, 66, 67]. Analytical spiral trajectory design methods are typically restricted to certain types of spirals, such as Archimedian spiral [68-70] or a polynomial spiral [71], whose density is proportional to an arbitrary power of radius. For arbitrary density spiral, a generalized Archimedian formula [72] and numerical method [73] are available. While such designs successfully achieve the desired density over most of the sampled k-space, the density near the origin is usually higher than is desired due to gradient amplitude and slew rate limits. Also, the distance between adjacent spiral paths, which determines the density of the sample, depends not only on the desired density of that sample, but also on the integration of the desired density over the radial distance. To overcome these limitations, we present here a variable-density, interleaved spiral trajectory numerical design method with arbitrary radial density under the condition that we acquire at least four angular interleaves for all the slices. The condition of a minimum number of interleaves is not a limiting constraint in practice for the sampling problems that we address. For faster implementation of this design, we propose simplified density-calculation method compared to the conventional Voronoi-based method [74] and show that the result matches with the density based on Voronoi areas. The k-space trajectory traversal makes optimal use of the gradient and slew limit constraints.

In addition to achieving large lipid suppression from the filter design, we further enhance this suppression during data reconstruction by exploiting the fact that the source of the strong undesired signal is limited to the subcutaneous tissues, but with no lipids arises from the brain itself. Similar ideas have been proposed in the literature, including dual-density sampling [75],

which reduces the truncation artifact by acquiring additional data in the high spatial k-space and a selective reconstruction to estimate the high spatial resolution spectra in the region of lipid and the low spatial resolution spectra of the brain. Other extrapolation methods [76-78] estimate the high spatial-resolution lipid spectra and reduce truncation artifacts and undesired signal leakage into the brain using a prior or data-driven knowledge of the lipid mask or the boundary of the brain or the scalp and subcutaneous tissues.

In our approach to post-acquisition lipid suppression we have developed the iterative non-linear reconstruction method that imposes the spatially-bound source of the lipid signals that often appear as artifacts in spectra inside the brain. The method is built on high-quality prior knowledge about the location of the periphery of the brain (acquisition of such data is integral to the MRI scan and comes without overall scan time penalty). The method utilizes a basis of lipid spectra that are acquired from the MRSI data themselves with very high SNR and aims to minimize the lipid contributions inside the brain, as defined by the mask, calculated by the inner product of the spectra in the voxel to the basis of the lipid spectra. To form a basis of the lipid spectra, we collect the spectra on the lipid mask estimated using the MRSI data themselves, with filtering to remove the residual water component. Compared to the extrapolation method [27], our approach does not need an accurate definition of a spatial lipid sources other than to impose that they arise from outside the brain mask.

The iterative reconstruction starts with the initial estimate of the spectra determined by the conventional linear reconstruction method (zero-padding and inverse Fourier transforms). The reconstruction criterion is regularized by the lipid contributions inside the brain, represented as an inner product of the spectra inside the brain to the basis of the lipid spectra. For each iterative step, the basis of the lipid spectra is selected by the spatial and spectral mask. Then, the spectra are updated by the steepest descent approach.

4.2 METHODS

In the following sections, we present the isotropic filter design method that minimizes the lipid contamination inside the brain, variable density spiral trajectory design method for arbitrary but smooth radial sampling density profile, and a non-linear iterative reconstruction method to further reduce the within-brain lipid contamination.

4.2.1 Real Time Isotropic Filter Design Algorithm for Lipid Suppression inside the Brain

We developed a real time procedure of MRSI scans shown in Figure 19 to reduce the lipid contamination inside the brain. In this section, we present the filter design method that minimizes the lipid contamination inside the brain using prior data acquired by pre-scans.

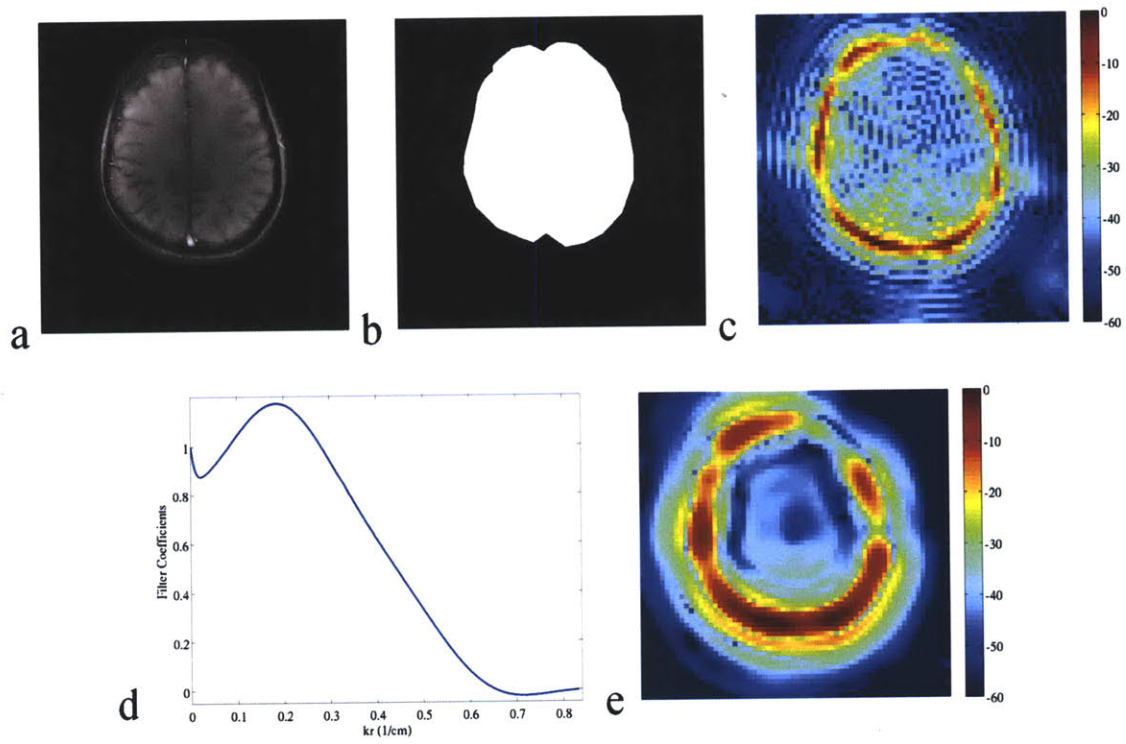

Figure 69: Flow of real time filter design and MRSI scans: (a) Step 1: acquire a high spatial resolution gradient echo image, (b) Step 2: estimate the brain mask, (c) Step 3: acquire a high spatial resolution MRSI pre-scan to estimate the lipid amount for any filter with a smaller k-space extent and the lipid amount in dB scale is shown, (d) Step 4: Design the filter, (e) Step 5: Scan spiral MRSI scan whose density is proportional to the filter designed and in this figure the lipid amount in dB scale is shown.

The isotropic filter design method minimizes the energy of the lipid contamination inside the brain given a k-space extent (i.e. maximum radius of sampling in k-space) and a voxel size. This filter is applied to the imaging data as a window or an apodization function (i.e. it multiplies the k-space data prior to Fourier transform to the image domain) on the uniform grid in k-space. The extent of the filter in the k-space matches the extent of the k-space trajectory and determines the number of nonzero filter coefficients. In general, to achieve a smaller voxel size (i.e. higher spatial resolution) requires a larger extent in the k-space that imposes cost in terms of spatial encoding time. The isotropic filter has radial symmetry, i.e. its coefficients are only function of k-space radius, and thus the number of independent nonzero filter coefficients is the number of distinct radii on the uniform grid within the sampled extent.

The voxel size, V , can be calculated as an inverse of the area of the normalized filter coefficients in the k-space [79]: $V = FOV_{xyz} / \sum_r f_r \cdot n_r$, where f_r is the filter coefficient at radius r in k-space, and n_r is the number of points in the uniform grid of the k-space at radius r. The sum is over the entire set of k-space points within the sampled k-space radius. For normalization, the filter coefficient in the k-space origin is fixed to a value of one. This formula for the voxel size is meaningful only if the point spread function (PSF) of the filter decays sufficiently fast. Otherwise, the signal accumulated to one voxel is not just from the voxel itself and next to it but can be from voxels not close to it. Then, more signals are added on the voxel in the middle of the brain than the voxel close to the boundary. In this case, the voxel size, the amount of accumulated signal in one voxel, of water or NAA inside the brain is not uniform. We have constrained the amplitude of PSF in more than 3cm away to be very small. This PSF constraint can be expressed in a matrix form as $\|W_{sl} f\|_2^2 < \varepsilon_{sl}$ .The voxel size condition, described above, can be summarized in a matrix form as

$$f^H n = FOV_{xyz} / V \text{ , } f(1) = 1 \text{ , and } \|W_{sl} f\|_2^2 < \varepsilon_{sl} .$$

To estimate the lipid response of our filter inside the brain we collect two additional pre-scans. To estimate the mask of the brain we collect a structural image with a high resolution gradient echo image (GRE) using the same slice thickness, the same Field of View (FOV) but with the

very short acquisition time (5 seconds). To estimate and simulate the lipid response, we acquire and the spiral MRSI, using the same TE as the metabolite scan but with the higher extent and shorter TR. Then the lipid response of the metabolite scan can be simulated by multiplying the isotropic filter to the pre-scan data. The lipid response of the isotropic filter can be written as a linear combination of the lipid response of each independent filter coefficient. Each response can be determined by the Discrete Fourier Transform (DFT) of the signal obtained by setting the corresponding parameter to one and zero elsewhere, i.e. one at a certain radius and zero otherwise. With those responses we can represent the lipid response inside the brain as a multiplication of the matrix, F_s, whose column is the response of each independent coefficient, and of the vector of independent filter coefficients, f. In other words, the lipid response, g_s, can be represented as $g_s = F_s f$.

An additional constraint we considered on the filter coefficients is smoothness. To maximize the SNR we design the spiral trajectory whose density is proportional to the filter coefficients. Since the k-space trajectory is controlled by gradient and slew limit, it is difficult to design the spiral with a non-smooth density. We impose the smoothness constraint of the filter as

$$\sum |f(i) - f(i+1)|^2 < \varepsilon_s,$$

which can be rewritten in a matrix form as $\|W_s f\|_2^2 < \varepsilon_s$, where W_s is an $m \times m$ matrix whose entries are all zero except $W_s(i,i) = 1$ for all $1 \le i \le m$ and $W_s(i,i+1) = -1$ for all $1 \le i \le m-1$, and m is the number of entries in the vector f.

Finally, we design the filter that minimizes the energy of the lipid inside the brain with the extent, the voxel size and the smoothness constraints:

Find f that minimizes $f^H F_s^H F_s f + \lambda_s f^H W_s^H W_s f + \lambda_{sl} f^H W_{sl}^H W_{sl} f$ such that $f^H n = FOV_{xyz} / V$ and $f(1) = 1$.

4.2.2 Variable Density Interleaved Spiral Trajectory Design Algorithm

In this section, we present an algorithm to design the variable-density spiral trajectory in k_x and k_y corresponding to the filter we designed in the previous section. As it is shown in [6, 66, 67], the SNR is maximized when the k-space sampling density is proportional to the coefficient of the filter. To maximize the SNR, the desired density of the spiral trajectory is chosen to be proportional to the coefficients of the filter but to be more than or equal to the Nyquist sampling rate (1/FOV). The spiral trajectory starts at the origin, $k_x = 0$, $k_y = 0$, and after all of its samples are acquired, it rewinds back to the origin followed by additional zeros padded to achieve the desired period chosen to have a sufficient bandwidth in the spectral domain. The rewound and zero-padded spiral lobe is repeated for the duration of the readout period.

For any arbitrary trajectory, the Voronoi method [74] can be used to estimate the density of the non-uniformly spaced k-space samples, which in general is a function of both radius and angle in k-space. To obtain a radially symmetric density estimate, we simplified this method by approximating the Voronoi area (inverse of the density) as the area of the ring divided by the number of angular interleaves (See eq. 1. below) [80]. This simplified density calculation method is a good match to the Voronoi density calculation as long as the number of angular interleaves is sufficiently large. Unlike the Voronoi method, the simplified radial-density calculation is independent of the angle of the samples in the trajectory. Figure 20 demonstrates that the normalized density calculated from the simple method (the red line) is approaching the normalized density from the Voronoi method (the blue line) as we increase the number of angular interleaves.

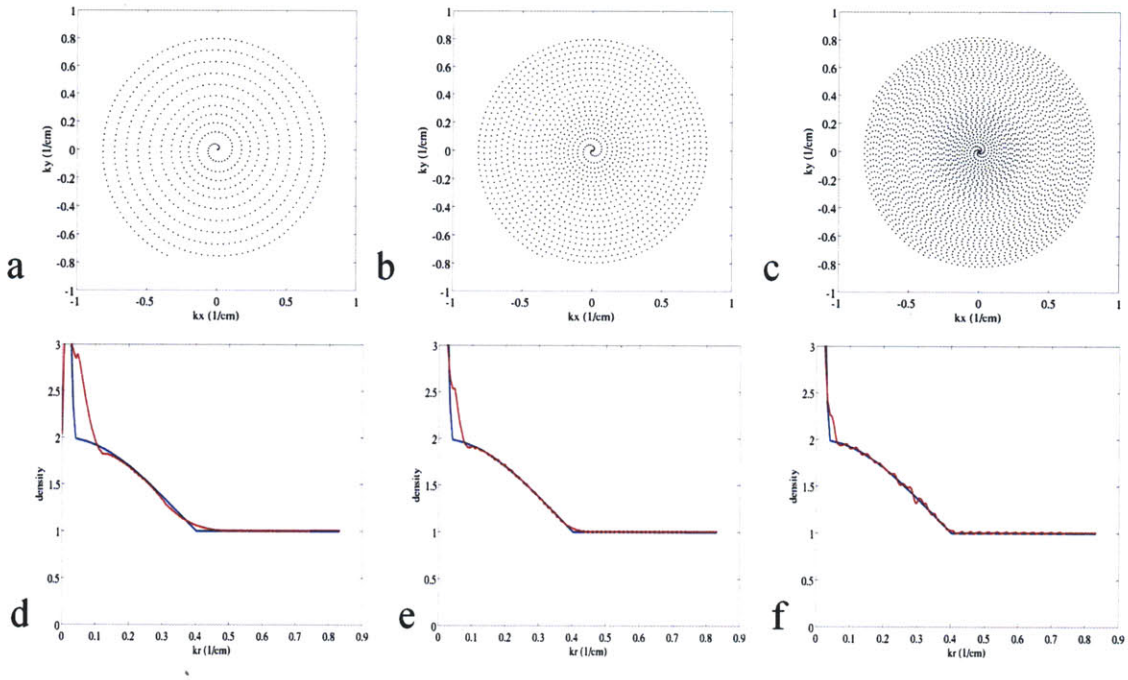

Figure 70: (a-c) Spiral trajectory used with 1, 2, 4 angular interleaves combined, (d-f) The density calculated from the simple radial method (blue line) and Voronoi method (red line)

Based on this density approximation method, we can now design a trajectory with the desired density profile in three steps shown in Figure 21: 1) generate the 2D PR (Projection reconstruction) trajectory that achieves the desired density, 2) connect the k-space origin to the k-space sample of the smallest radius in the 2D PR trajectory within gradient and slew limits, 3) Rotate the trajectory as fast as it can within the gradient and slew limits.

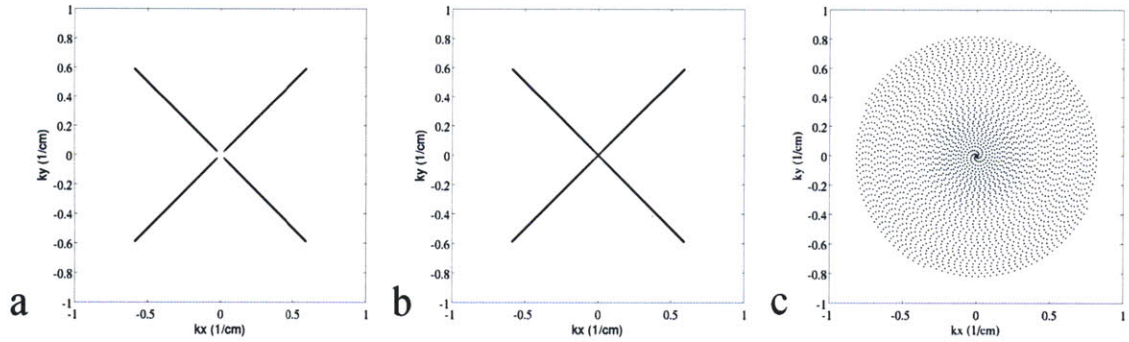

Figure 21: Three steps of designing spiral trajectory with the desired density profile, (a) Step 1: 2D PR with desired density, (b) Step 2: Connect k-space origin to the 2D PR trajectory within gradient and slew limits, (c) Step 3: Rotate the trajectory within gradient and slew limits

For simplicity, we will use the following notation and equations in the rest of this section.

Notation and Equations

N_A : The number of angular interleaves,

N : The number of samples,

$r[n]$, $\theta[n]$: The radius and the angle of the trajectory at the nth sample,

$b[n]$: The average radius of two consecutive samples, $r[n-1]$, $r[n]$,

$$b[0] = 0, \; b[n] = (r[n] + r[n-1]) / 2,$$

$A[n]$: The Voronoi area of the nth sample, $A[n] = \pi(b[n+1]^2 - b[n]^2) / NA$, (1)

$V_A(r)$: The desired Voronoi area at radius r,

FOV : Field of view in x and y,

T : The sampling period,

$G_{\max}$: The maximum gradient,

$S_{\max}$: The maximum slew rate.

$b[n] = \sqrt{b[n+1]^2 - N_A V_A(r[n]) / \pi}$, $r[n-1] = 2r[n] - b[n]$, (2)

$$\left|r[n+1]\exp\{j(\theta[n+1]-\theta[n])\}-r[n]\right| \le \min(1/FOV,\ \gamma TG_{\max}/2\pi), \quad (3)$$

$$\left|r[n+2]\exp\{j(\theta[n+2]-\theta[n])\}-2r[n+1]\exp\{j(\theta[n+1]-\theta[n])\}+r[n]\right| \le \gamma T^2 S_{\max}/2\pi. \quad (4)$$

1. Radius Calculation (Step 1+2)

The largest radius, $r[N]$, in the spiral trajectory matches the desired extent of the trajectory, whereas the radius of the previous sample, $r[N-1]$, is determined to achieve the Nyquist rate, $1/FOV$, of the sampling density. The radii of the other samples are calculated in a descending order. For each sample, the radius of the sample is calculated to match the desired Voronoi density (eq. 2). This process is repeated until the calculated radius of the previous sample becomes less than zero or greater than the current sample. We start the k-space trajectory in the k-space origin but the smallest calculated radius is not usually zero. We add several initial samples to connect the origin to the smallest radius. Typically fewer than 10 samples are added to satisfy the gradient and slew limit. This is a minor adjustment to the trajectory design and negligible effects on the density and SNR.

2. Angle Calculation (Step 3)

After we have calculated the radii of the trajectory, we determine the angle of the k-space samples in an ascending order. In each sample, we calculate the possible ranges of the change in the angle, $\theta[n+1]-\theta[n]$, that satisfy the gradient limit and Nyquist rate (eq. 3.), the slew limit of the previous sample (eq. 4.) as well as the slew limit the current sample itself so that it is possible to locate the next sample within the slew limit (eq. 4.). Here we choose the maximum value in the range.

4.2.3 Iterative Non-Linear Reconstruction

To condition the iterative reconstruction and impose the spatial prior of the brain, we have used the brain mask estimated in the real time filter design method. Low resolution receive coil sensitivity map is collected in the beginning of the MRSI scan and interpolated to match with the

MRSI data. The high resolution GRE image provides a high-quality spatial prior for spatial localization of skull, subcutaneous fat and brain. We process this image and generate a spatial lipid mask, i.e. of skull as well as subcutaneous fat, as well as a separate brain mask. The receive coil profile is used for coil combination in MRSI weighted by the conjugate of the receive coil sensitivity, which is optimal for Independent, Identically distributed (I.I.D.) noise [81].

The raw data sampled on the spiral trajectory are processed by a gridding reconstruction method [37] in the (k_x, k_y)-plane with a Kaiser-Bessel kernel and an oversampling factor of 2. Then the isotropic filter is applied on the post-gridded data before performing the iterative non-linear reconstruction method. As an initialization of the iterative process, we perform the conventional linear reconstruction method, which involves zero-padding to the nearest power of two inverse FFT, and a coil combination. In each iterative step, the spectra within the lipid mask are collected and spectrally masked from 2.7 ppm to 5.9 ppm to remove any residual water component in the spectra. The water-masked lipid spectra form a basis set that is used in the MRSI reconstruction by minimizing the cost function:

$$\sum_k \left\| F_u I_k - d_k \right\|_2^2 + \lambda \sum_{x,y \in M_b} \sum_l \left\| s_l' s_c(x,y) \right\|_1 ,$$

where I_k is the MRSI image from coil k, F_u is Fourier operator on the sampled MRSI extent, d_k are post-gridded raw data from coil k, M_b is the brain mask, s_l are lipid spectra from the basis of the lipid, and s_c are the spectra in the combined MRSI image. The first term in this expression enforces data consistency, while the second term minimizes lipids inside the brain mask. We minimize the cost function by a steepest descent algorithm implemented in Matlab. That is, we calculate the gradient of the minimizing criterion in the direction of I_k and update the I_k along the direction of the gradient.

Two healthy volunteers, after signing consent form, were scanned on a 3T Siemens Tim Trio scanner with a 32-channel head coil. The following series were acquired: 1. Three-plane localizer (FOV_{xy} = 250 mm, slice thickness = 7 mm, resolution = 512*512, TE = 4 ms, TR = 8.6 ms, TA = 12s), 2. Scout for mask image, a high resolution GRE (FOV_{xy} = 240 mm, slice thickness = 10 mm, resolution = 512*512, TE = 3.81 ms, TR = 9.9 ms, TA = 5s, flip angle = 20°), 3. Spin Echo MRSI scan for lipid map (FOV_{xy} = 240 mm, slice thickness = 10 mm, voxel

size = 0.2 cm^3, TE = 144ms, TR = 1000 ms, TA = 52s, flip angle = 20°), 4. Three spin Echo MRSI scans for metabolite maps (FOV_{xy} = 240 mm, slice thickness = 10 mm, voxel size = 1.5 cm^3, TE = 144ms, TR = 2000 ms, TA = 104 s). The scout and spin echo MRSI scans were selective excitation of the head in an axial section with the slice thickness of 10mm. For MRSI data, conventional Chess water suppression was used but no additional RF pulses to suppress the lipid were used. To estimate the location of the brain, the scout, a high resolution GRE, image was collected and then we manually drew the boundary of the brain. In addition to this, we collected the high resolution lipid maps by constant density spiral trajectory MRSI scan with the same TE (144 ms) as the MRSI scan, but the shorter TR of 1000 ms and the higher k-space extent spatially. Sensitivity map of the receive coils was acquired in the beginning of the MRSI scan by using the pre-scan procedure of the Siemens protocol. The total scan time for these pre-scans including the B0 shimming process was about two minutes. With these pre-scans we were able to simulate the lipid response in the mask of the brain for any filter.

Then we designed the isotropic filter that minimizes the lipid contamination inside the brain. The computation of the optimal filter was processed on a separate Linux machine. The entire process, including copying the pre-scan data to the machine, drawing the boundary of the brain manually, computing the filter, and copying the filter back to the host of the MR scanner, took about five minutes. While designing the optimal filter, we collected two additional spin echo spiral-MRSI scans with a constant density corresponding to the no-apodization and a variable density spiral MRSI scan whose density is proportional to the pre-calculated 1D Equiripple filter. The specifications of the spin echo MRSI scans included the TE of 144ms, the TR of 2000 ms, the scan time of 104 s, the voxel size of 1.5 cm^3, the slice thickness of 10 mm in an axial section, and the FOV_{xy} of 240 mm. The extent of the trajectories and the apodization were adjusted to match the voxel size. These data were used to compare the performance of the lipid contamination given the same voxel size and imaging time. Finally, we collected the MRSI spectra through the variable density spiral trajectory corresponding to the optimal filter coefficients.

To quantify the of lipid suppression of our method, we estimated the lipid map as the sum of the absolute value of the spectra from 0.9 ppm to 1.7 ppm. These data were processed by the conventional linear reconstruction process, which consisted of gridding, FFT and coil combination. Then, we performed the proposed iterative reconstruction method to further reduce the lipid contamination

4.3 RESULTS

By applying the optimal filter, we gained about 10dB of the lipid suppression compared to the no-apodization and the 1D Equiripple filter and we achieved about 30~40 dB suppression of the lipid inside the brain as it is shown in Figure 22.

Figure 22 and 23 shows the estimated lipid maps using the pre-scan, the high spatial resolution spiral CSI with a short TR, and the acquired lipid maps by the spin echo MRSI scans in dB scale in Figure 22 and in linear scale in Figure 23. The pre-scan does not have a good SNR for the metabolites but has a good SNR for lipid. The spatial side-lobe ringing of the lipid can be simulated for any arbitrary apodization with a smaller k-space extent. As it is shown in Figure 22 and 23, the estimated lipid maps can be used to predict the acquired lipid maps.

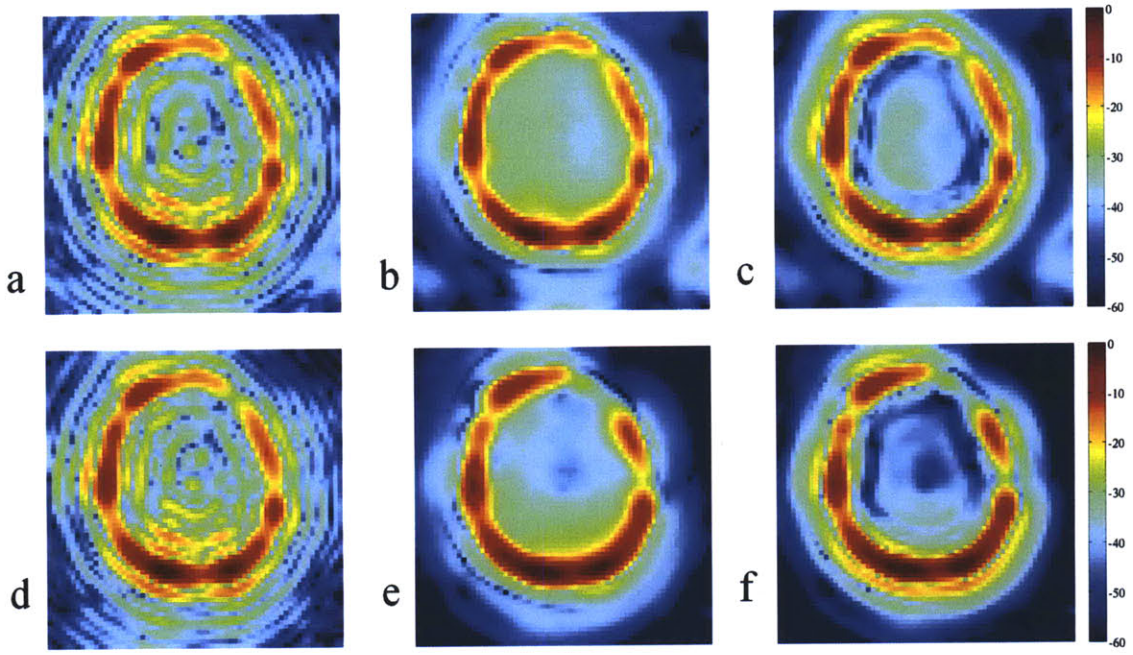

Figure 22: Normalized Lipid Amount in dB scale (the sum of absolute value of the spectra from 0.9 ppm to 1.7 ppm), reconstructed by the conventional method: (a-c) Estimated data using the pre-scan data, (d-f) Acquired data using spin echo spiral MRSI sequence

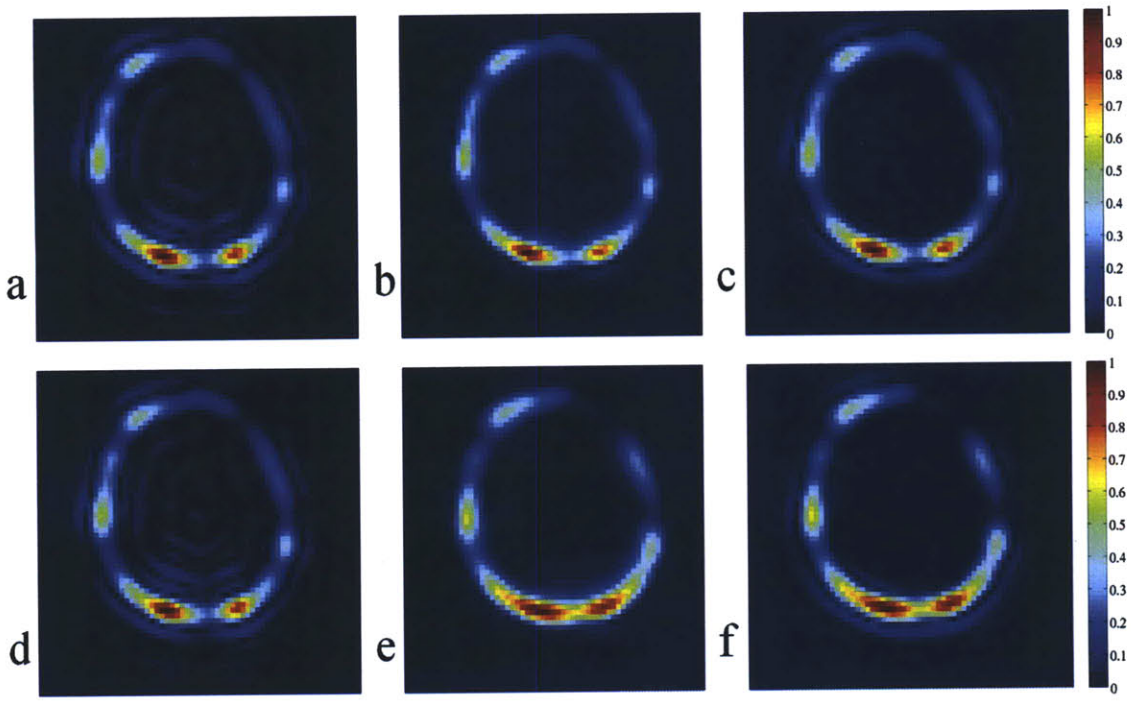

Figure 23: Normalized Lipid Amount in linear scale (the sum of absolute value of the spectra from 0.9 ppm to 1.7 ppm), reconstructed by the conventional method: (a-c) Estimated data using the pre-scan data, (d-f) Acquired data using spin echo spiral MRSI sequence

In Figure 24, the spectra of the NAA, Cr, Cho, and lipid from 1.2 ppm to 3.8 ppm in the yellow rectangle indicated in Figure 24(d) are shown.

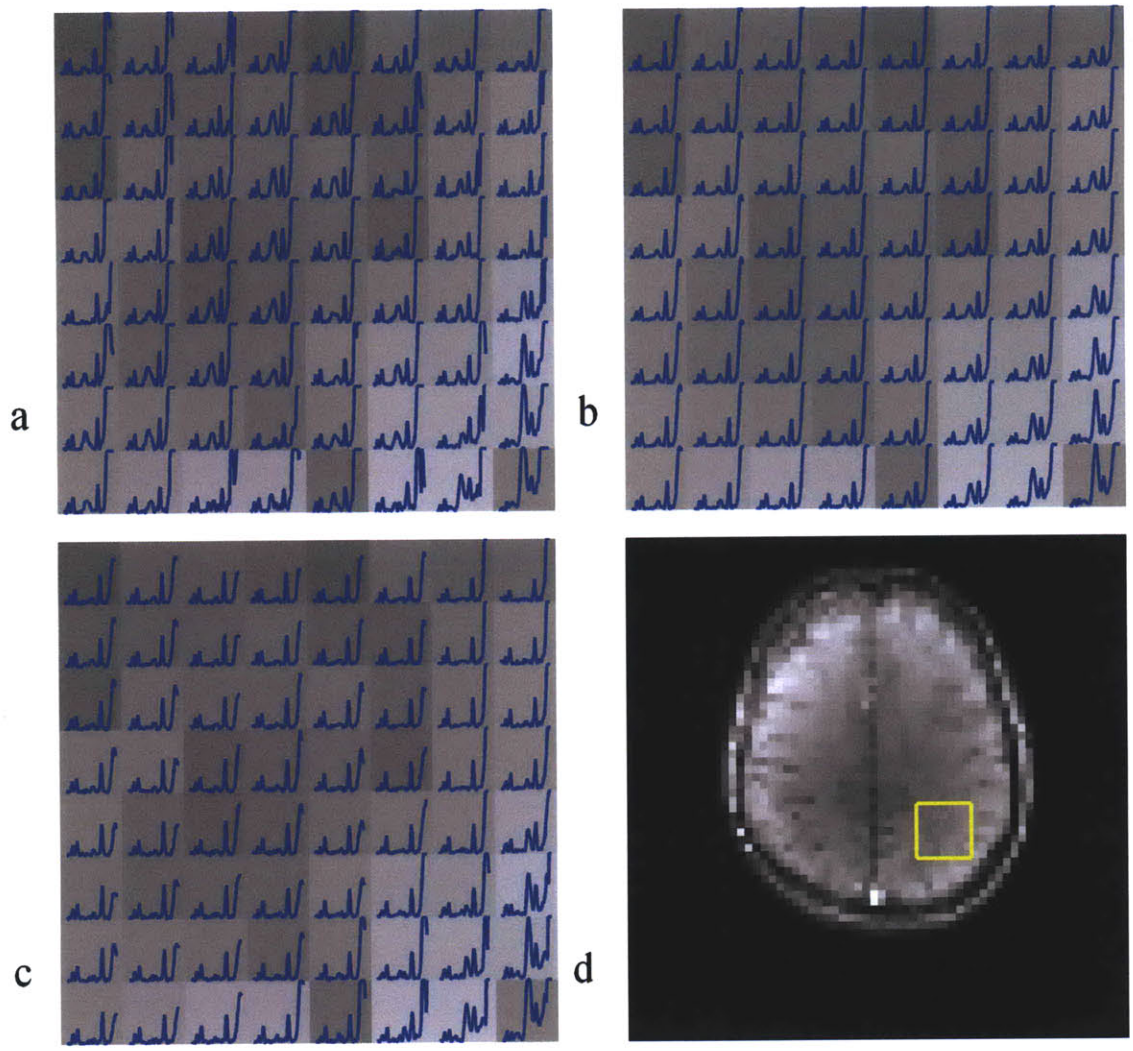

Figure 24: Spectra of the NAA, Cre, Cho, and lipid (1.2 ppm ~3.8 ppm) inside the yellow rectangle in (d): (a) No Apodization, (b) 1D Equiripple Filter, (c) Real Time Filter, (d) Underlying Structural image (Gradient Echo Image) of the same slice

We performed the proposed iterative reconstruction method to reduce the lipid contamination on the spectra corresponding to the real time filter. As it is shown in Figure 25, we gained additional 10~20 dB suppression of the lipid contamination inside the brain.

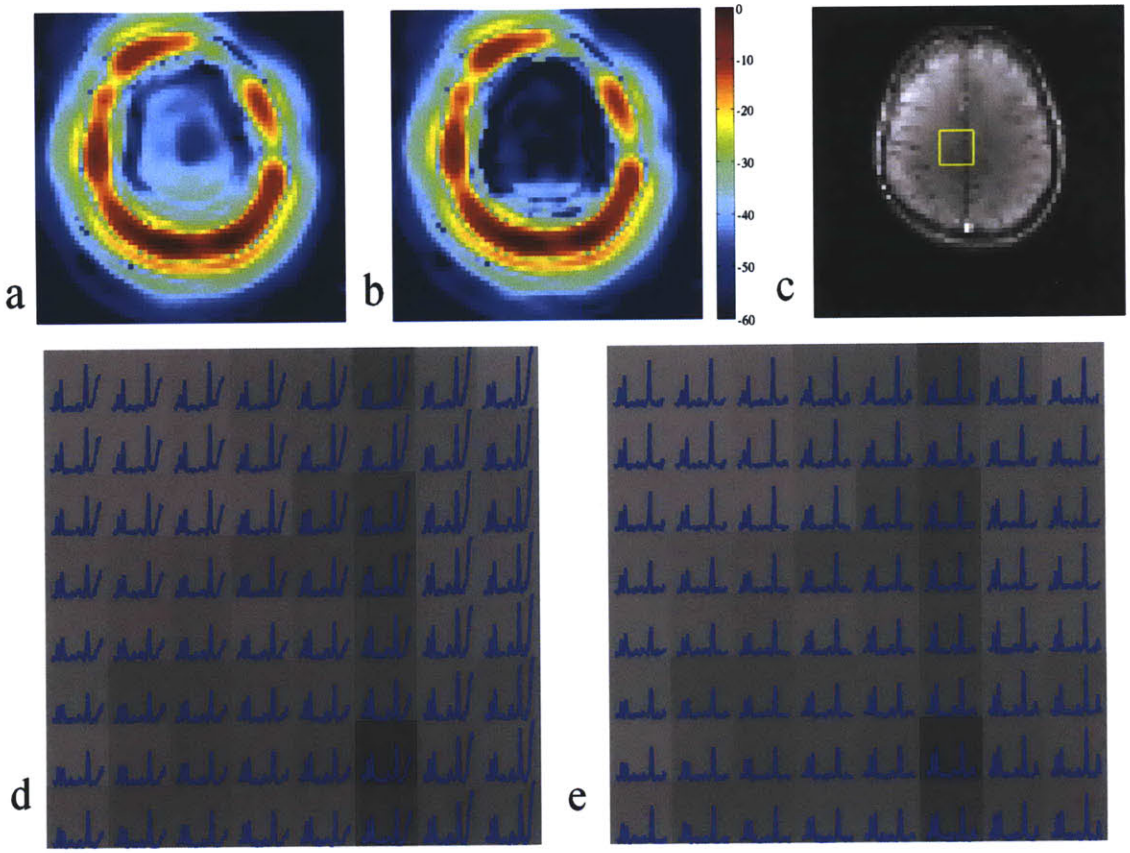

Figure 25: Lipid map and (a-b) the spectra (d-f) of the conventional reconstruction and iterative reconstruction methods inside the yellow rectangle the gradient echo image (c): (a) Lipid Map: Conventional Reconstruction, (b) Lipid Map: Iterative Reconstruction, (c) Gradient Echo Image, (d) Spectra (NAA, Cre, Cho) from the conventional reconstruction, (d) Spectra (NAA, Cre, Cho) from the iterative reconstruction

In Figure 26, the spectrum of a voxel (third row and fifth column of the spectra in 7 (d-e) is shown. Lipid spectra were greatly reduced and the spectra of residual water, Cr and Cho were not changed by the iterative reconstruction method. Our iterative reconstruction took about 5 minutes to estimate the spectra from the individual receive coil of the 32 channel head coil and the combined spectra. The specification of the imaging size included 64*64 spatially and 256 spectrally.

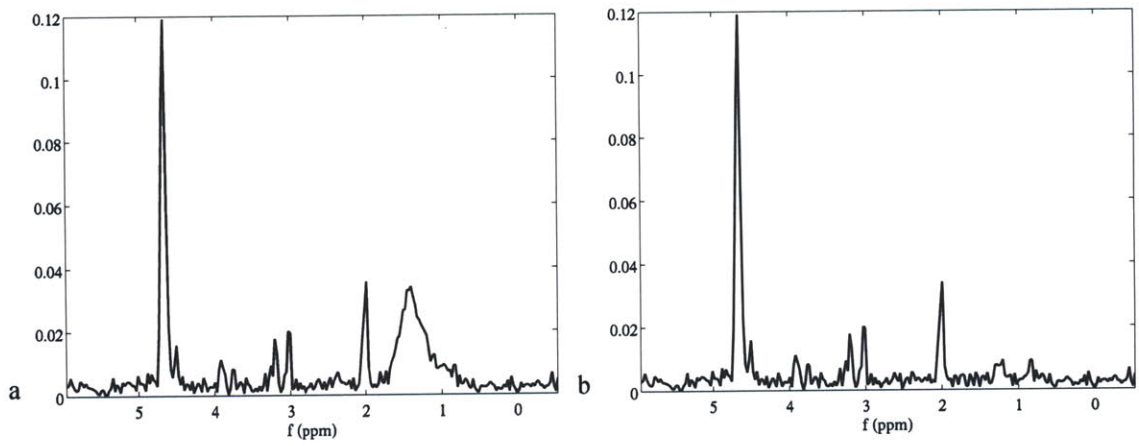

Figure 26: Spectrum of one voxel in magnitude, third row and fifth column of the spectra in Figure 25 (d-e): (a) Conventional Reconstruction, (b) Iterative Reconstruction

4.4 Discussions and Conclusions

We presented a design method for an isotropic filter to minimize the lipid contamination inside the brain by measuring an additional high spatial resolution lipid scan. To maximize SNR, we propose a method for a variable-density spiral trajectory, whose density is proportional to the filter coefficients. Even in the absence of other means of lipid suppression, such as outer-volume suppression or inversion recovery, this method can spatially confine the source of the contaminating lipid signals to regions outside of the brain to achieve 30~40 dB lipid suppression in cortical brain spectra without a tradeoff in metabolite SNR. The apodization also serves to reduce spatial ringing in the metabolite maps and limits the spatial extent of other undesired signals, such as undesired residual water, especially from CSF in the middle of the brain, shown in Figure 27.

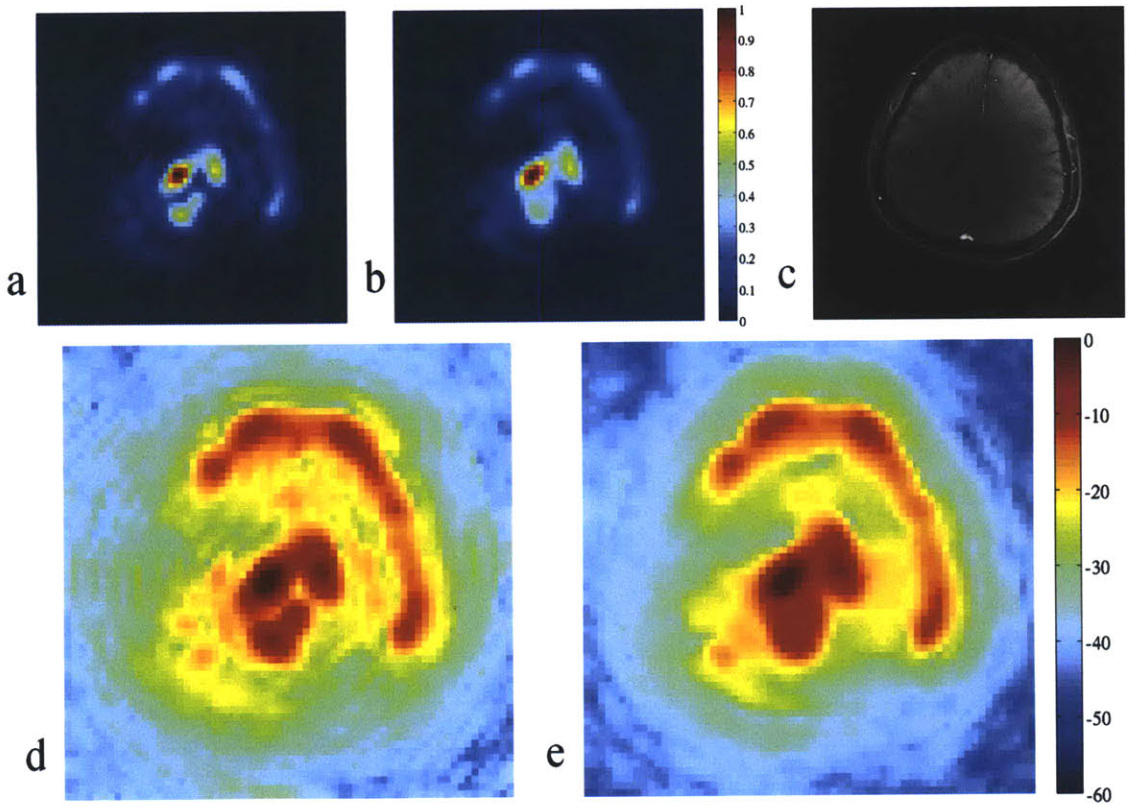

Figure 27: Undesired residual water in linear scale (a-b) and dB scale: (a) No apodization in linear scale, (b) Real time filter in linear scale, (c) Gradient echo image of the same slice, (d) No apodization in dB scale, (e) Real time filter in dB scale

With the iterative non-linear reconstruction process, we can further reduce the lipid contamination in the brain with an additional 10~20 dB suppression. Data collection by a single slice MRSI of normal volunteers demonstrated the performance of the method in terms of lipid suppression and metabolite SNR. This method is particularly useful for improved brain metabolite detection and quantification in the cortex of the brain.

Chapter 5

Summary and Future Work

5.1 Summary

In this work, we developed and demonstrated novel methods for challenging problems in MRI RF excitation for parallel transmission at high field, as well for as lipid suppression in spectroscopic imaging. The proposed excitation methods developed for 7T parallel transmit system aim to overcome critical current constraints of high field systems for human imaging and make it feasible deploy this emerging platform for use in clinical and research experiments with MRI and MRSI.

5.2 Contributions

The main contributions of this work are summarized below:

5.2.1 B1+ and B1- mapping for pTx at 7T [38]

- Developed a fast B1+ and B1- mapping method for eight channel pTx system at 7T by optimally combining the B1+ of the eight transmit coils in an adaptive fashion

- Validated the B1+ and B1- method by comparing the Bloch simulation and the measured flip angle of pTx RF pulses
- Proposed a compressed sensing (CS) method for B1+ mapping that utilizes the smoothness (sparsity) of B1+ map. This method can be used for several magnitude-based B1+ mapping techniques such as double-angle method [16, 19], multi-angle method [11, 17], saturation angle method [20, 46]
- Implemented the CS approach for B1+ mapping for the saturation angle method [46]

5.2.2 Integration of peak local-SAR minimization in pTx RF design [82, 83]

- Realized a heuristic approach of the model compression technique for peak local SAR calculation [84] to dramatically decrease the complexity of the peak local SAR calculation with respect to the number of voxels involved
- Proposed a generic iterative pTx pulse design method that regularizes the peak 10g local SAR
- Evaluated the performance of iterative pTx pulse design method for magnitude least squares (MLS) spoke design [13] and arbitrary excitation for spiral trajectory [8] , and achieved ~20-40% decrease in peak local SAR compared to the conventional methods

5.2.3 Lipid suppression in MRSI [85-88]

- Proposed a real time procedure to minimize artifacts due to lipid contamination in brain MRSI
- Designed an optimal spatial filter by using mild priors, such as a spatial brain mask and high resolution lipid image collected before the MRSI scan, and demonstrated the performance of this approach for in-vivo subjects, where 30~40dB suppression of within-brain lipids were achieved with a voxel size of 1.5 cm^3.
- By adopting a simple density calculation method [80], we developed a simple variable-density interleaved spiral trajectory design method for arbitrary radial density profile, which was critical to implement the SNR-maximized lipid suppression where sampling density is constrained to be proportional to the applied apodization function.

- Developed a nonlinear iterative post-processing method of MRSI that further reduces the lipid contamination inside the brain and achieved 10~20dB additional suppression of artifacts.

5.3 Future Work

The list below provides several logical extensions to the work presented in this thesis.

5.3.1 B1+ and B1- mapping for pTx at 7T

- Use pTx pulse design methods such as MLS spokes [13] in order to further decrease the maximum-to-minimum ratio of the combined mode and thereby increase the SNR of the B1+ estimate
- Generalize the proposed method as demonstrated for single-slice mapping, and implement it for volumetric or multi-slice B1+ and B1- mapping
- We expect the compressed sensing method to yield high acceleration factors for volumetric B1+ and B1- mapping with even higher acceleration than we demonstrated for 2D since 3D allows for acceleration along additional direction, z

5.3.2 pTx pulse design with a local SAR constraint

- Expand the local-SAR minimization to include two or more pTx RF pulses, or a sequence of pTx RF pulses, to jointly minimize the time-averaged peak local SAR. These RF pulses will be played periodically in a series of TRs and all examples of such sequences have been demonstrated to achieve approximately the same B1+ mitigation while achieving lower peak local SAR than a repeat application of a single pTx pulse [89].

5.3.3 Lipid suppression in MRSI

- Demonstrate the proposed method for short TE MRSI where the lipid suppression problem is more challenging due to short T2 of lipids compared to brain metabolites.
- Implement a multi-slice MRSI extension of the currently demonstrated single-slice method, which could contain up to four slices within the same TR of 2s.
- Generalize the real-time filter design for lipid suppression to volumetric MRSI
- Incorporate sparse sampling with compressed-sensing reconstruction for enhanced lipid reconstruction based on the spatial and spectral lipid prior.

Bibliography

1. Soares, D.P. and M. Law, *Magnetic resonance spectroscopy of the brain: review of metabolites and clinical applications.* Clin Radiol, 2009. **64**(1): p. 12-21.
2. Stanwell, P. and C. Mountford, *In vivo proton MR spectroscopy of the breast.* Radiographics, 2007. **27 Suppl 1**: p. S253-66.
3. Bartella, L. and W. Huang, *Proton (1H) MR spectroscopy of the breast.* Radiographics, 2007. **27 Suppl 1**: p. S241-52.
4. Kurhanewicz, J. and D.B. Vigneron, *Advances in MR spectroscopy of the prostate.* Magn Reson Imaging Clin N Am, 2008. **16**(4): p. 697-710, ix-x.
5. Gray, H. and W.H. Lewis, *Anatomy of the human body*. 1918, Philadelphia; New York: Lea & Febiger.
6. Macovski, A., *Noise in MRI.* Magn Reson Med, 1996. **36**(3): p. 494-7.
7. Schoenberg, S.O., et al. *Parallel imaging in clinical MR applications*. [SpringerLink] 2007; xii, 560 p.].
8. Setsompop, K., et al., *Parallel RF transmission with eight channels at 3 Tesla.* Magn Reson Med, 2006. **56**(5): p. 1163-71.
9. Setsompop, K., et al., *High-flip-angle slice-selective parallel RF transmission with 8 channels at 7 T.* J Magn Reson, 2008. **195**(1): p. 76-84.
10. Setsompop, K., et al., *Broadband slab selection with B1+ mitigation at 7T via parallel spectral-spatial excitation.* Magn Reson Med, 2009. **61**(2): p. 493-500.
11. Setsompop, K., et al., *Slice-selective RF pulses for in vivo B1+ inhomogeneity mitigation at 7 tesla using parallel RF excitation with a 16-element coil.* Magn Reson Med, 2008. **60**(6): p. 1422-32.
12. Alagappan, V., et al., *Degenerate mode band-pass birdcage coil for accelerated parallel excitation.* Magn Reson Med, 2007. **57**(6): p. 1148-58.
13. Setsompop, K., et al., *Magnitude least squares optimization for parallel radio frequency excitation design demonstrated at 7 Tesla with eight channels.* Magn Reson Med, 2008. **59**(4): p. 908-15.
14. Brunner, D.O. and K.P. Pruessmann, *Optimal design of multiple-channel RF pulses under strict power and SAR constraints.* Magn Reson Med, 2010. **63**(5): p. 1280-91.
15. Yarnykh, V.L., *Actual flip-angle imaging in the pulsed steady state: a method for rapid three-dimensional mapping of the transmitted radiofrequency field.* Magn Reson Med, 2007. **57**(1): p. 192-200.

16. Stollberger, R. and P. Wach, *Imaging of the active B1 field in vivo.* Magn Reson Med, 1996. **35**(2): p. 246-51.
17. Kerr, A.B., et al. *Self-Calibrated Transmit SENSE.* in *14th Annual Meeting of ISMRM* 2006. Seattle, Washington, USA.
18. Dowell, N.G. and P.S. Tofts, *Fast, accurate, and precise mapping of the RF field in vivo using the 180 degrees signal null.* Magn Reson Med, 2007. **58**(3): p. 622-30.
19. Cunningham, C.H., J.M. Pauly, and K.S. Nayak, *Saturated double-angle method for rapid B1+ mapping.* Magn Reson Med, 2006. **55**(6): p. 1326-33.
20. Brunner, D.O., S. Schweizer, and K.P. Pruessmann. *Fast mapping of highly inhomogeneous RF fields.* in *15th Annual Meeting of ISMRM.* 2007. Berlin, Germany.
21. Sacolick, L.I., et al., *B1 mapping by Bloch-Siegert shift.* Magn Reson Med, 2010. **63**(5): p. 1315-22.
22. Morrell, G.R., *A phase-sensitive method of flip angle mapping.* Magn Reson Med, 2008. **60**(4): p. 889-94.
23. Adalsteinsson, E., et al., *Volumetric spectroscopic imaging with spiral-based k-space trajectories.* Magn Reson Med, 1998. **39**(6): p. 889-98.
24. Bowtell, R., et al., *Proton chemical-shift mapping using PREP.* Journal of Magnetic Resonance (1969), 1989. **82**(3): p. 634-639.
25. Doyle, M. and P. Mansfield, *Chemical-shift imaging: a hybrid approach.* Magn Reson Med, 1987. **5**(3): p. 255-61.
26. Guilfoyle, D.N., et al., *PEEP--a rapid chemical-shift imaging method.* Magn Reson Med, 1989. **10**(2): p. 282-7.
27. Haase, A., *Snapshot FLASH MRI. Applications to T1, T2, and chemical-shift imaging.* Magn Reson Med, 1990. **13**(1): p. 77-89.
28. Haase, A. and D. Matthaei, *Spectroscopic FLASH NMR imaging (SPLASH imaging).* Journal of Magnetic Resonance (1969), 1987. **71**(3): p. 550-553.
29. Macovski, A., *Volumetric NMR imaging with time-varying gradients.* Magn Reson Med, 1985. **2**(1): p. 29-40.
30. Mansfield, P., *Spatial mapping of the chemical shift in NMR.* Magn Reson Med, 1984. **1**(3): p. 370-86.
31. Matsui, S., K. Sekihara, and H. Kohno, *High-speed spatially resolved NMR spectroscopy using phase-modulated spin-echo trains. Expansion of the spectral bandwidth by combined use of delayed spin-echo trains.* Journal of Magnetic Resonance (1969), 1985. **64**(1): p. 167-171.
32. Sepponen, R.E., J.T. Sipponen, and J.I. Tanttu, *A method for chemical shift imaging: demonstration of bone marrow involvement with proton chemical shift imaging.* J Comput Assist Tomogr, 1984. **8**(4): p. 585-7.
33. Twieg, D.B., *Acquisition and accuracy in rapid NMR imaging methods.* Magn Reson Med, 1985. **2**(5): p. 437-52.
34. Twieg, D.B., *Multiple-output chemical shift imaging (MOCSI): a practical technique for rapid spectroscopic imaging.* Magn Reson Med, 1989. **12**(1): p. 64-73.
35. Twieg, D.B., J. Katz, and R.M. Peshock, *A general treatment of NMR imaging with chemical shifts and motion.* Magn Reson Med, 1987. **5**(1): p. 32-46.
36. Webb, P., D. Spielman, and A. Macovski, *A fast spectroscopic imaging method using a blipped phase encode gradient.* Magn Reson Med, 1989. **12**(3): p. 306-15.

37. Beatty, P.J., D.G. Nishimura, and J.M. Pauly, *Rapid gridding reconstruction with a minimal oversampling ratio.* IEEE Trans Med Imaging, 2005. **24**(6): p. 799-808.
38. Lee J., et al. *Fast B1+ mapping with Validation for parallel transmit system in 7T.* in *18th Annual Meeting of ISMRM* 2010. Stockholm, Sweden.
39. Malik, S.J., D.J. Larkman, and J.V. Hajnal, *Optimal linear combinations of array elements for B1 mapping.* Magn Reson Med, 2009. **62**(4): p. 902-9.
40. Nehrke, K., *On the steady-state properties of actual flip angle imaging (AFI).* Magn Reson Med, 2009. **61**(1): p. 84-92.
41. Lustig, M., D. Donoho, and J.M. Pauly, *Sparse MRI: The application of compressed sensing for rapid MR imaging.* Magn Reson Med, 2007. **58**(6): p. 1182-95.
42. Gebhardt M., et al. *Evaluation of maximum local SAR for parallel transmission (pTx) pulses based on pre-calculated field data using a selected subset of "Virtual Observation Points".* in *18th Annual Meeting of ISMRM.* 2010. Stockholm, Sweden.
43. Adalsteinsson, E., et al., *Reduced spatial side lobes in chemical-shift imaging.* Magn Reson Med, 1999. **42**(2): p. 314-23.
44. Gumbrecht R., et al. *Fast high-flip pTx pulse design to mitigate B1+ inhomogeneity using composite pulses at 7T.* in *18th Annual Meeting of ISMRM* 2010. Stockholm, Sweden.
45. Lee J., et al. *Parallel Transmit RF Design with Local SAR Constraints.* in *18th Annual Meeting of ISMRM* 2010. Stockholm, Sweden.
46. Fautz, H.-P., et al. *B1 mapping of coil arrays for parallel transmission.* in *16th Annual Meeting of ISMRM.* 2008. Toronto, Canada.
47. Funai, A., et al. *REGULARIZED B1+ MAP ESTIMATION IN MRI.* in *Biomedical Imaging: From Nano to Macro, 2007. ISBI 2007. 4th IEEE International Symposium on.* 2007.
48. Chung, S., et al., *Rapid B1+ mapping using a preconditioning RF pulse with TurboFLASH readout.* Magnetic Resonance in Medicine, in press.
49. Wiggins, G.C., et al. *An 8 Channel Phase Array Coil and Detunable TEM Transmit Coil for 7T Brain Imaging.* in *12th Annual Meeting of ISMRM.* 2004. Kyoto, Japan.
50. Mao, W., M.B. Smith, and C.M. Collins, *Exploring the limits of RF shimming for high-field MRI of the human head.* Magn Reson Med, 2006. **56**(4): p. 918-22.
51. Grissom, W., et al., *Spatial domain method for the design of RF pulses in multicoil parallel excitation.* Magn Reson Med, 2006. **56**(3): p. 620-9.
52. Taflove, A. and S.C. Hagness, *Computational electrodynamics : the finite-difference time-domain method.* 2nd ed. 2000, Boston: Artech House. xxiii, 852 p.
53. *IEEE Recommended Practice for Measurements and Computations of Radio Frequency Electromagnetic Fields With Respect to Human Exposure to Such Fields, 100 kHz-300 GHz.* IEEE Std C95.3-2002 (Revision of IEEE Std C95.3-1991), 2002: p. i-126.
54. Christ, A., et al., *The Virtual Family-development of surface-based anatomical models of two adults and two children for dosimetric simulations.* Physics in Medicine and Biology, 2010. **55**(2): p. N23-N38.
55. Duyn, J.H., et al., *Multisection proton MR spectroscopic imaging of the brain.* Radiology, 1993. **188**(1): p. 277-82.
56. Le Roux, P., et al., *Optimized outer volume suppression for single-shot fast spin-echo cardiac imaging.* J Magn Reson Imaging, 1998. **8**(5): p. 1022-32.
57. Luo, Y., et al., *BISTRO: an outer-volume suppression method that tolerates RF field inhomogeneity.* Magn Reson Med, 2001. **45**(6): p. 1095-102.

58. Tran, T.K., et al., *Very selective suppression pulses for clinical MRSI studies of brain and prostate cancer.* Magn Reson Med, 2000. **43**(1): p. 23-33.
59. Bydder, G.M. and I.R. Young, *MR imaging: clinical use of the inversion recovery sequence.* J Comput Assist Tomogr, 1985. **9**(4): p. 659-75.
60. Ebel, A., V. Govindaraju, and A.A. Maudsley, *Comparison of inversion recovery preparation schemes for lipid suppression in 1H MRSI of human brain.* Magn Reson Med, 2003. **49**(5): p. 903-8.
61. Spielman, D.M., et al., *Lipid-suppressed single- and multisection proton spectroscopic imaging of the human brain.* J Magn Reson Imaging, 1992. **2**(3): p. 253-62.
62. Bottomley, P.A., *Spatial localization in NMR spectroscopy in vivo.* Ann N Y Acad Sci, 1987. **508**: p. 333-48.
63. Spielman, D., et al., *1H spectroscopic imaging using a spectral-spatial excitation pulse.* Magn Reson Med, 1991. **18**(2): p. 269-79.
64. Balchandani, P. and D. Spielman, *Fat suppression for 1H MRSI at 7T using spectrally selective adiabatic inversion recovery.* Magn Reson Med, 2008. **59**(5): p. 980-8.
65. Parker, D.L., G.T. Gullberg, and P.R. Frederick, *Gibbs artifact removal in magnetic resonance imaging.* Med Phys, 1987. **14**(4): p. 640-5.
66. Brooker, H.R., T.H. Mareci, and J.T. Mao, *Selective Fourier transform localization.* Magn Reson Med, 1987. **5**(5): p. 417-33.
67. Mareci, T.H., Brooker HR., *High-resolution magnetic resonance spectra from a sensitive region defined with pulsed field gradients.* J Magn Reson, 1984. **57**: p. 157-163.
68. Cline, H.E., X. Zong, and N. Gai, *Design of a logarithmic k-space spiral trajectory.* Magn Reson Med, 2001. **46**(6): p. 1130-5.
69. Glover, G.H., *Simple analytic spiral K-space algorithm.* Magn Reson Med, 1999. **42**(2): p. 412-5.
70. Meyer, C.H., et al., *Fast spiral coronary artery imaging.* Magn Reson Med, 1992. **28**(2): p. 202-13.
71. Kim, D.H., E. Adalsteinsson, and D.M. Spielman, *Simple analytic variable density spiral design.* Magn Reson Med, 2003. **50**(1): p. 214-9.
72. Lee, J.H., et al., *Fast 3D imaging using variable-density spiral trajectories with applications to limb perfusion.* Magn Reson Med, 2003. **50**(6): p. 1276-85.
73. Hargreaves, B.A., http://mrsrl.stanford.edu/~brian/vdspiral.
74. Rasche, V., et al., *Resampling of data between arbitrary grids using convolution interpolation.* IEEE Trans Med Imaging, 1999. **18**(5): p. 385-92.
75. Sarkar, S., K. Heberlein, and X. Hu, *Truncation artifact reduction in spectroscopic imaging using a dual-density spiral k-space trajectory.* Magn Reson Imaging, 2002. **20**(10): p. 743-57.
76. Haupt, C.I., et al., *Removal of lipid artifacts in 1H spectroscopic imaging by data extrapolation.* Magn Reson Med, 1996. **35**(5): p. 678-87.
77. Metzger, G., et al., *A hybrid technique for spectroscopic imaging with reduced truncation artifact.* Magn Reson Imaging, 1999. **17**(3): p. 435-43.
78. Plevritis, S.K. and A. Macovski, *MRS imaging using anatomically based k-space sampling and extrapolation.* Magn Reson Med, 1995. **34**(5): p. 686-93.
79. Hanson, L.G., *Fast Volumetric Magnetic Resonance Spectroscopic Imaging.* Ph.D thesis, University of Copenhagen, Denmark, 1999.

80. Pauly, J. *course note, Stanford Univ.,* http://www.stanford.edu/class/ee369c/notes/non_cart_rec_07.pdf.
81. Pruessmann, K.P., et al., *Advances in sensitivity encoding with arbitrary k-space trajectories.* Magn Reson Med, 2001. **46**(4): p. 638-51.
82. Lee J., et al. *Parallel Transmit RF Design with Local SAR Constraints.* in *18th Annual Meeting of ISMRM.* 2010. Stockholm, Sweden.
83. Lee J., et al., *Local SAR Constrained RF Design for Parallel Transmission in Magnetic Resonance Imaging, MGH Case No. 20770, US Patent Pending.* 2010.
84. Matthias G., et al. *Evaluation of maximum local SAR for parallel transmission (pTx) pulses based on pre-calculated field data using a selected subset of "Virtual Observation Points".* in *18th Annual Meeting of ISMRM.* 2010. Stockholm, Sweden.
85. Lee J. and E. Adalsteinsson. *Three-Dimensional Isotropic Filter Design with Arbitrary Pass-Band and Stop-Band Specifications.* in *16th Annual Meeting of ISMRM.* 2008. Toronto, Canada.
86. Lee J., Gagoski B., and E. Adalsteinsson. *Lipid suppression with variable-density spiral trajectory for volumetric brain CSI* in *16th Annual Meeting of ISMRM.* 2008. Toronto, Canada.
87. Lee J., et al. *Subcutaneous lipid suppression via variable-density spiral sampling for full cortical coverage in chemical shift imaging.* in *17th Annual Meeting of ISMRM.* 2009. Honolulu, Hawaii, USA.
88. Lee J. and E. Adalsteinsson. *Iterative CSI Reconstruction with High-Resoluiton Spatial Priors for Improved Lipid Suppression.* in *18th Annual Meeting of ISMRM.* 2010. Stockholm, Sweden.
89. Zelinski, A.C. and Massachusetts Institute of Technology. Dept. of Electrical Engineering and Computer Science., *Improvements in magnetic resonance imaging excitation pulse design.* 2008. p. 253 p.